Politecnico di Torino

Corso di Laurea Magistrale in Ingegneria Energetica e Nucleare

EIT InnoEnergy Master in Environomical Pathways for Sustainable Energy Systems (SELECT)

Tesi di Laurea Magistrale

Characterization and Optimization of Organic Solar Cells for Agrivoltaic Applications

Supervisor:
Prof. Federico Bella

Candidate:
Jonas Auth

Internal Supervision at ISE:
Dr. Uli Würfel
Dr. Birger Zimmermann
Leonie Pap

In collaboration with
Fraunhofer Institute for Solar Energy Systems

October 2024

Contents

List of Figures

List of Tables

Abstract

One of the distinctive features of organic solar cells is the ability to selectively absorb light within specific wavelength ranges. For that reason they can be designed to mainly absorb light outside the visible spectrum, while simultaneously transmitting visible wavelengths. This ability makes them a perfect fit for semi-transparent applications such as tinted windows and agrivoltaics.
In agrivoltaic applications, it is important to reach a sufficient transparency level, in order to minimize negative effects on plant growth. This transparency can be quantified by the growth factor, which represents the weighted percentage of light transmitted through the cell, based on the wavelengths that are most relevant for plant growth. While the requirements vary for different plant species, a minimum growth factor of 60 % is recommended to support the growth of a variety of plants, for example, basil. The main goal of this work is to evaluate materials and develop a stack configuration that can reach this targeted growth factor.

In this process several absorber materials were analyzed for their compatibility to achieve such a high growth factor. Afterwards stack configurations were developed using the best suited blend, PV-X Plus, as the absorber material. The main feature of these stacks is the back electrode that was designed to maximize the reflection of near-infrared (NIR) light back into the absorber material, while transmitting visible light. This was done using several layers of metal oxides and other materials to form a dielectric Bragg reflector (DBR). The layer thicknesses for each material were optimized using the transfer-matrix method (TMM) in a Python-based code, to maximize the growth factor. The results of the simulations were then experimentally recreated.

As a result a growth factor of $G = 61.6\,\%$ and a power conversion efficiency (PCE) of 3.5 % were experimentally achieved. The study demonstrates the potential to use semi-transparent organic solar cells for agrivoltaic applications. It also indicates, that the most limiting factor, to further improve the transparency and power conversion efficiency, remains the absorber material.

Chapter 1

Introduction: Global Energy Context

The modern world faces increasing challenges related to the human-made climate change. This development is mainly driven by our increase in energy consumption during the last century. Some significant effects that can be observed globally are an increase in extreme weather events, like hurricanes, droughts, and floods [1].

Even in Europe, where these effects are relatively small, the faster melting of glaciers and the increase in stronger heatwaves are noticeable. These changes impact both human health and agriculture [1]–[3].

Depending on the scenario in the World Energy Outlook 2023, the global energy demand will continue to rise or slightly decline. The scenarios, namely Stated Policies Scenario (STEPS), Announced Pledges Scenario (APS), and Net Zero Emissions by 2050 Scenario (NZE), differ mainly in terms of their policy and technological adoption rates. Nevertheless, Figure 1.1 shows an increase in electricity demand in all three scenarios, pointing out the need to further expand renewable electricity production [4].

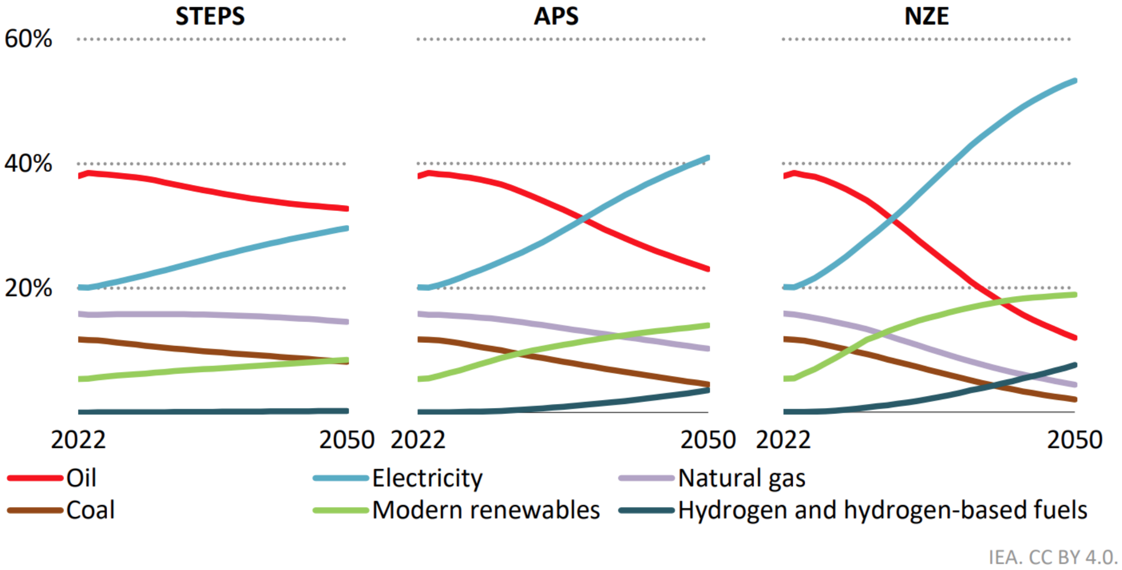

Figure 1.1: Global energy demand by technology in the three different scenarios STEPS, APS and NZE. All three scenarios show a sharp increase in electricity demand for the next decades. Retrieved from the World Energy Outlook 2023 [4].

This expansion is also complicated by geopolitical tensions related to fossil fuels and the scarcity of minerals that are essential for the energy transition and defence sector [5].

Critical minerals such as lithium, cobalt, and rare earth elements are not easily replaceable for most renewable technologies. The following Figure 1.2 illustrates some specific minerals that are critical for those [6].

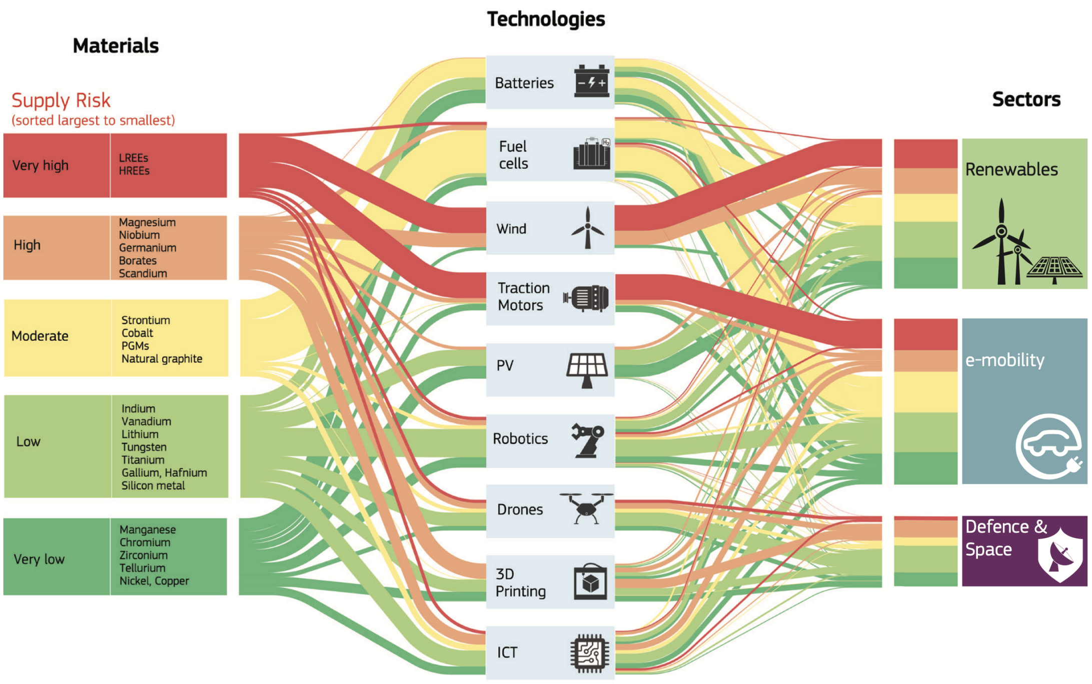

Figure 1.2: Flow of materials, categorized by supply risk, into technologies and their application in the sectors Renewables, E-mobility, and Defence & Space. Thicker lines indicate a higher dependence. Retrieved from [6].

Although Europe is deploying a lot of renewable energy technologies and maintains strong in research [7], the supply of essential minerals makes us reliant on other countries. Figure 1.3 illustrates the global dependence on supply chains for these new technologies, particularly highlighting the significant reliance on China [8].

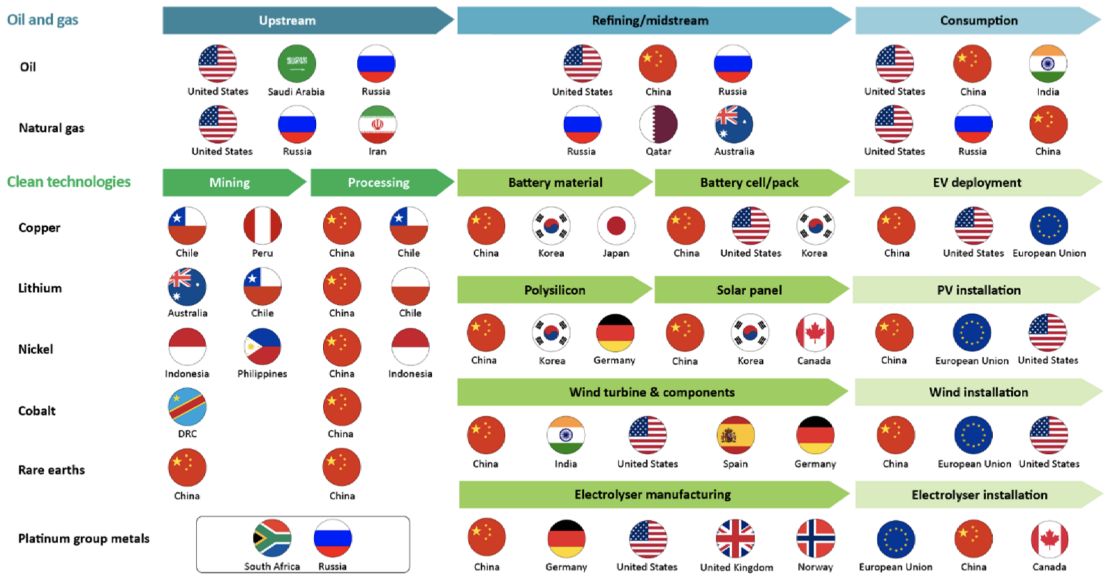

Figure 1.3: Supply chain illustration for energy transition technologies, highlighting the dependence on China. Retrieved from [8].

The current renewable technologies like wind, silicon based solar, and hydro power have and will continue to make a significant impact on the energy transition. After all, their expansion is limited to factors like the availability of suitable area, reliance on critical materials, and their environmental impact during production [6], [9], [10]. Given these limitations, there is a need to expand our renewable energy portfolio by investing in new technologies that address them.

This thesis proposes to explore the improvement of semi-transparent organic solar cells (ST-OSC). Unlike in inorganic materials such as crystalline silicon, the absorption coefficient does not necessarily increase with higher photon energies. Thus it is possible to modify the molecular structure of such an organic material, in order to efficiently absorb near-infrared light while remaining semi-transparent in the visible region. Additionally, these materials can be used to fabricate lightweight, flexible, and solution-processed solar cells, which makes them suitable for a wide range of applications [11], [12].

1.1 State of the Art - Solar Cells

In comparison to silicon-based solar cells, organic solar cells have a reduced manufacturing footprint and have a lower toxicity for the environment [13].
On the other hand Figure 1.4 shows that the power conversion efficiencies (PCE) for organic solar cells and other emerging technologies are still behind that of silicon-based photovoltaics. Considering this, it is challenging for them to compete in traditional applications like rooftop or open space photovoltaics. Nevertheless, the ongoing research is promising and rapid improvements in efficiency were observed during the last decades.

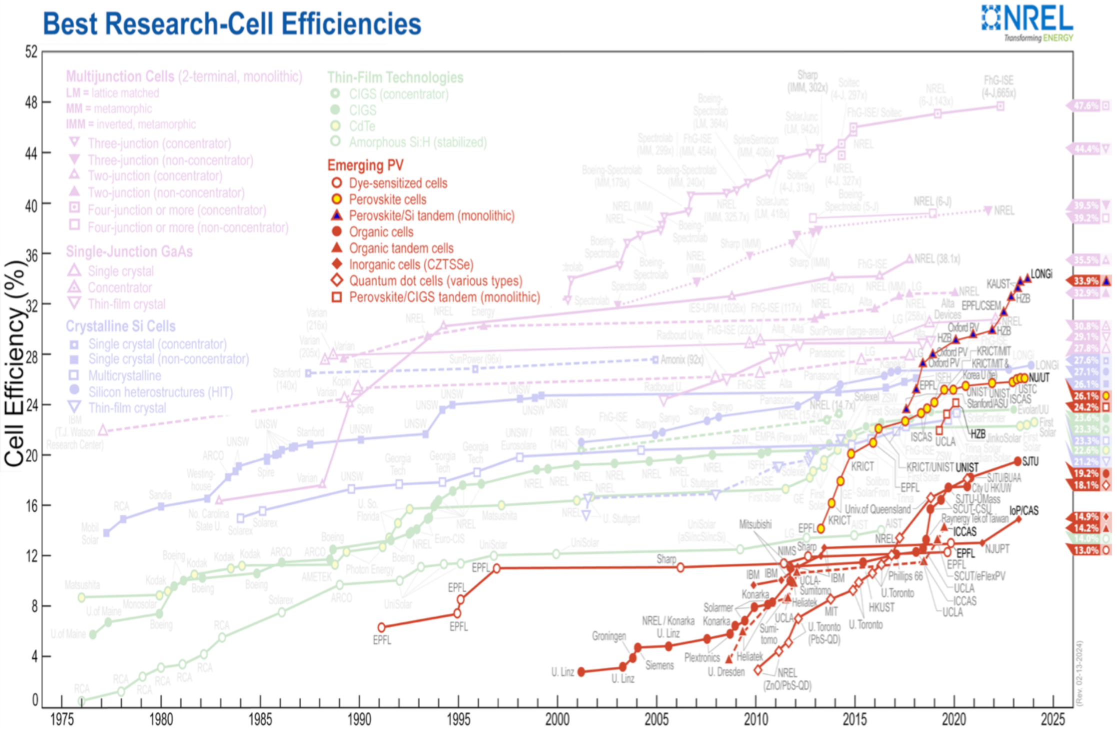

Figure 1.4: Evolution of solar cell efficiencies for different technologies. Showing a rapid increase in PCE for OSCs over the last decade. Retrieved from [14].

However, in specific applications, these technologies offer some benefits. For instance, organic solar cells can be built on flexible substrates, which allows them to be integrated into wearable technology and deployed on irregular surfaces [15], [16]. Additionally, their active area can be semi-transparent, making them ideal for the use in windows or in agrivoltaic systems [12], [17], [18].

This thesis will focus on the development of organic solar cells specifically for the application in Agrivoltaics. Research in this specific areas is limited and a measurable characteristic is also not well established, thus a direct comparison between different papers is often not possible. In this thesis a weighted transparency referred to as growth factor or average photosynthetic transmittance is chosen to evaluate the transparency. The growth factor represents the weighted percentage of light transmitted through the cell, based on the wavelengths that are most relevant for plant growth. It will be explained in more detail in Section 3.

Previous studies considering the specific application in agriculture and using the growth factor as a characteristic have achieved a PCE of 7.75 % and a plant growth factor of 24.8 % [19]. Another study showed a even higher performance with a PCE of 13.02 % and a growth factor of 26.3 % [20]. Both studies prioritized efficiency over transparency, while the focus in this work will be specifically on transparency.

1.2 Scope of the Thesis

The scope of the thesis focuses on the "Characterization and Optimization of Organic Solar Cells for Agrivoltaic Applications". The goal is, by optimizing the absorber materials and the solar cell stack, to reach a growth factor (G) of over 60 %. Experimental data and simulations are used to design the stack for an optimized layer absorption and transparency of the photoactive material, with a clear focus on reaching the transparency target. The assessment of long-term stability, upscaling to module size of the solar cells or the actual impact on the growth of a specific plant is beyond the scope of this work.

The research involves the construction of single cells, measuring their IV-curve characteristics under AM 1.5G conditions, and computing the growth factor using ultraviolet-visible spectroscopy (UV-VIS) data. To simulate their maximum possible short circuit current density (J_{sc}) and full stack transparency based on the UV-VIS data of each material, the transfer matrix method is utilized. Other advanced characterization techniques are only used for specific applications, such as determining the mismatch factor for the J_{sc} measurements or analyzing certain specific aspects of the cell like the external quantum efficiency (EQE). These techniques are however not used for each measurement run.

A special focus is to use materials that provide a more sustainable option compared to conventional inorganic solar cells and to make use of underutilized areas, specifically agricultural fields, that can serve a second purpose in energy production. The work, therefore, promotes a sustainable solution that can be used as an addition to the current spectrum of renewable energy sources to further assist in the global energy transition away from fossil fuels.

Chapter 2

Theory: Physical Principles of Solar Cells

The following section describes the theoretical fundamentals of organic solar cells. It starts with the physical principles including the photovoltaic effect, semiconductor properties and moves on with explaining the specifics related to organic semiconductors and organic solar cells. Finally, it describes the parameters necessary to characterize solar cells and more specifically semi-transparent organic solar cells.

Generally, solar cells are based on the fundamental principle of the photovoltaic effect. This effect describes the generation of electrical current in a material when it is exposed to light. When photons strike a material, they can transfer their energy to electrons within the material. If the energy of the photons is sufficient, the electrons are excited and transition from the valence band to the conduction band. As a consequence a positively charged hole remains in the valence band [21], [22].
Separating these charge carriers quickly is important in solar cell applications, for an effective energy conversion and to avoid recombination. This separation is more efficient in semiconductors than in metals, which makes them the preferred material for solar cells [23].

Semiconductor materials are used in transistors, diodes, solar cells, and other technologies that shape our modern society. Therefore, understanding the physical principles of semiconductor materials in general and for organic semiconductors in particular, is essential to understand the work presented in this master thesis.

2.1 Principles of Semiconductors

Metals and semiconductors absorb photons differently. Metals have a continuous range of electronic states, which allows them to absorb photons of any energy. On the other hand, they also release this energy again within picoseconds, in form of phonons. This makes it impossible to separate the charge carriers in time and use their energy externally [23].

In contrast, semiconductors have an energy gap between their valence and conduction bands. The valence band represents the highest energy range in which electrons are present at $T = 0\,\mathrm{K}$. While the conduction band represents the lowest range of unoccupied electronic states under this condition. In the valence band, electrons are mainly bound to their parent atoms and can only move around the crystal if a positive hole is available. However, once they transition to the conduction band, they are free to move, thereby enabling electrical conductivity [23].

In order to do this transition, the electrons have to absorb photons of energy at least equivalent to the bandgap. Photons with lower energy are not absorbed and are instead either transmitted or reflected. Once electrons are excited to the conduction band, they remain in these states long enough to be separated, allowing their energy to be converted into electrical energy [23].

2.1.1 Organic Semiconductors and Charge Carrier Generation

Organic semiconductors function similarly to conventional semiconductors but with some key differences. The term includes several types of materials, for example amorphous molecular films used in LEDs, molecular crystals used in transistors, and polymer films. Polymer films are particularly relevant for organic solar cells and will be explained in more detail [24].

These organic polymers are, in contrast to their inorganic counterparts, always carbon-based and mainly consist of carbon and hydrogen atoms. They can also include additional elements like sulfur, oxygen, and nitrogen. The polymers, that are relevant in the context of solar cells, usually consist of carbon atoms with alternating single and double bonds, and sometimes include aromatic rings [24].

In contrast to inorganic semiconductors, organic semiconductors do not form a band structure because the electrons are not delocalized over the entire material. Instead they are localized within single molecules. Therefore, the main defining energy levels are the highest occupied molecular orbital (HOMO) and the lowest unoccupied molecular orbital (LUMO), which are typically the binding and anti-binding π-orbitals [24].

When an organic material is exposed to light, it can form electron and hole pairs in a bound state called Frenkel excitons. They are in a bound state because there is not enough energy at room temperature to overcome the attractive Coulomb force between their opposite charges [23].
Equation 2.1 describes the ground state binding energy that holds the exciton together [23]:

$$E_{\text{exc}} = \frac{m_{\text{red}} e^4}{2(4\pi\epsilon\epsilon_0)^2 \hbar^2} \tag{2.1}$$

where m_{red} is the reduced mass of the exciton, $\hbar$ is Planck's constant, ϵ is the relative dielectric permittivity, and ϵ_0 is the dielectric permittivity of free space.

In inorganic semiconductors, where the binding energy of the exciton is smaller than kT at room temperature, the electrons and holes can move freely once they are exited. In contrast in organic semiconductors, the binding energy is higher than kT at room temperature, making the separation of charge carriers more difficult [23].

To overcome this binding energy, a combination of electron donors and acceptors is used to create a bulk heterojunction (BHJ) structure as shown in Figure 2.1 [25].

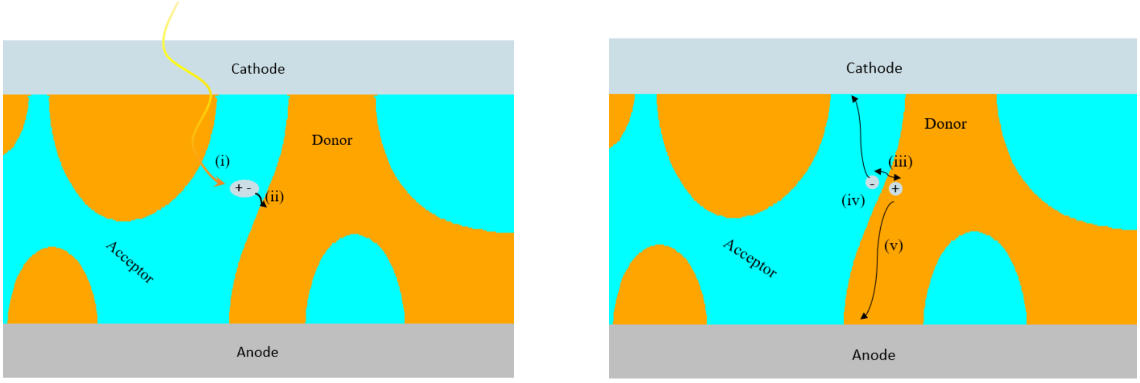

Figure 2.1: Illustration of the bulk heterojunction (BHJ) structure in organic solar cells. The left image shows the generation of Frenkel excitons after illumination, while the right image describes the process of exciton separation and charge carrier collection at the donor-acceptor interface. Adapted from [25]

Once the BHJ is illuminated, Frenkel excitons are generated (i). They now have to travel to the interface of donors and acceptors in order to separate into electrons and holes (ii). If the exciton diffusion length is lower than the distance to the interface or the separation is delayed, recombination can occur (iii) [25].
Therefore, high exciton diffusion lengths and a large interface area between donor and acceptor materials are important for efficient charge extraction [25]. The effects leading to an increased recombination rate will be explained in Section 2.1.2.
If the excitons reach the interface of acceptor and donor, and if the energy offset between those two is sufficient, they are split into free charge carriers (iv). Once electrons and holes are separated, they can move freely within their transport levels (v) and are collected at their respective electrodes (vi) [25].

2.1.2 Recombination in Solar Cells

In solar cells not all charge carriers that are exited by the incoming light can be extracted and used in an external circuit. There are several effects that might occur inside the cell that force the charge carriers to recombine. Under equilibrium conditions, without an external circuit, the rates of creation and annihilation of carriers are balanced and depend on the material properties. The energy released during recombination can be converted into photons or phonons, or sometimes both, depending on the mechanism, that is responsible [23].

The common types of recombination processes include:

Radiative Recombination is the reverse process of absorption, where a photon is emitted when an electron and a hole recombine. The radiative recombination rate depends on the probability of an electron encountering a hole. This rate is characterized by the radiative recombination coefficient (k_r) and depends also on the product of the electron and hole concentrations [23], [26].

$$R = k_r \cdot n_e \cdot n_h \tag{2.2}$$

where R is the radiative recombination rate, k_r is the radiative recombination coefficient, and n_e and n_h are the electron and hole concentrations [23], [26].

At the theoretical efficiency limit of a solar cell, only radiative recombination would occur. This limit is also known as the Shockley-Queisser limit, and is approximately $\text{PCE} = 33.7\,\%$ for a single-junction solar cell under AM 1.5G conditions [23], [24].

Auger Recombination is one of the non-radiative recombination effects next to trap-assisted recombination. In Auger recombination, the energy from an electron-hole recombination is transferred to a third charge carrier (electron or hole) in form of kinetic energy. This energy is then lost through collisions in the lattice as heat. The Auger recombination rate depends on the carrier concentrations, therefore on the doping of the material, and specific Auger coefficients for electrons (C_e) and holes (C_h) [23], [26].

Trap-Assisted Recombination occurs when impurities or defects in the semiconductor introduce energy states between the valence and conduction bands. Electrons or holes can be captured in these trap states and recombine by releasing the energy as heat [23], [26].

Surface Recombination is related to the trap-assisted recombination as these traps occur especially often at the surface or interface of a semiconductor. Surface recombination can be reduced by using a so called window layer which is a passivating layer with a large bandgap. This layer covers the semiconductor surface and reduces the number of available surface states [23], [26].

2.2 Organic Solar Cells

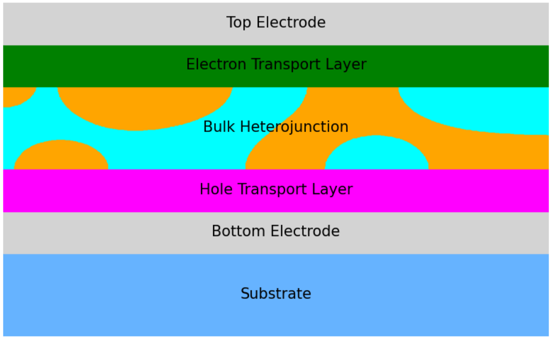

Figure 2.2: Schematic Representation of an Organic Solar Cell

Organic solar cells (OSC) are based on the fundamentals explained in the previous sections. They generally consist of two electrodes, a bulk heterojunction in the middle, and additional layers that enable the selective transport of charge carriers to their respective electrodes. The architecture of such a cell is illustrated in Figure 2.2 [27].
It is important to note that the structure can be reversed depending on the materials used for each layer and what is best for charge carrier collection and extraction.
Each layer of the organic solar cell has its dedicated function:

Glass Substrate: Serves as the main support layer to provide structural integrity. It can also be replaced with a flexible material.
Bottom Electrode: In the shown configuration it functions as the anode and is typically transparent. As a material indium tin oxide (ITO) is commonly used. Generally it is important that the material which is used collects and transports the charges effectively, while minimizing its impact on optical losses and electrical resistance [28].
Hole Transport Layer (HTL) and Electron Transport Layer (ETL): The ETL and HTL layers act as charge-selective membranes, meaning that they only let electrons or holes to the dedicated electrode [24], [27]. Ideally, if the energy levels are aligned properly, these layers help minimize recombination losses and improve charge extraction efficiency [24]. Therefore, they have energetically lower (for the ETL) or higher-lying LUMOs (for the HTL). The holes move from the donor's HOMO to the energetically preferable HOMO (or valence band, depending on the material) state in the HTL, while the electrons move from the acceptor's LUMO to the energetically preferable LUMO (or conduction band, depending on the material) of the ETL, as shown in Figure 2.3 [24].
Additionally, the ETL and HTL can physically improve the surface of the electrodes, passivate surface defects and pinholes and reduce leakage currents.

Photoactive Layer: Is composed of the donor and acceptor materials, typically in form of the BHJ. As explained in Section 2.1.1, when an exciton is created, it is separated by the difference in energy levels at the donor and acceptor interface. This difference is created through the energy offset between the energy levels of both materials as shown in Figure 2.3. The electron moves from the donor material to the acceptor material, while the hole remains within the transport levels of the donor. From here, the charge carriers move to their respective HTL or ETL layers [24].

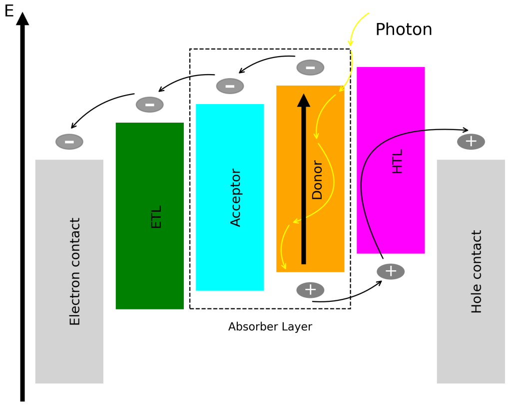

Figure 2.3: Schematic Energy Level Diagram of an OSC. Adapted from [24].

Top Electrode: In the shown configuration it functions as the cathode and is typically not transparent. Usually metals like aluminum or silver are used to effectively collect and transport the charges. For semi-transparent applications, a transparent electrode is beneficial, but options like a silver grid can also provide partial transparency and still collect the charges.

2.3 Characterization of Solar Cells

The following section describes the most important characteristics of a solar cell in order to quantify its behavior.

As discussed in the beginning of Section 2 the solar cell is a device that transforms photons into electrical energy. Some of the physical effects occurring during this process can be described with the equivalent circuit model shown in Figure 2.4 [23].

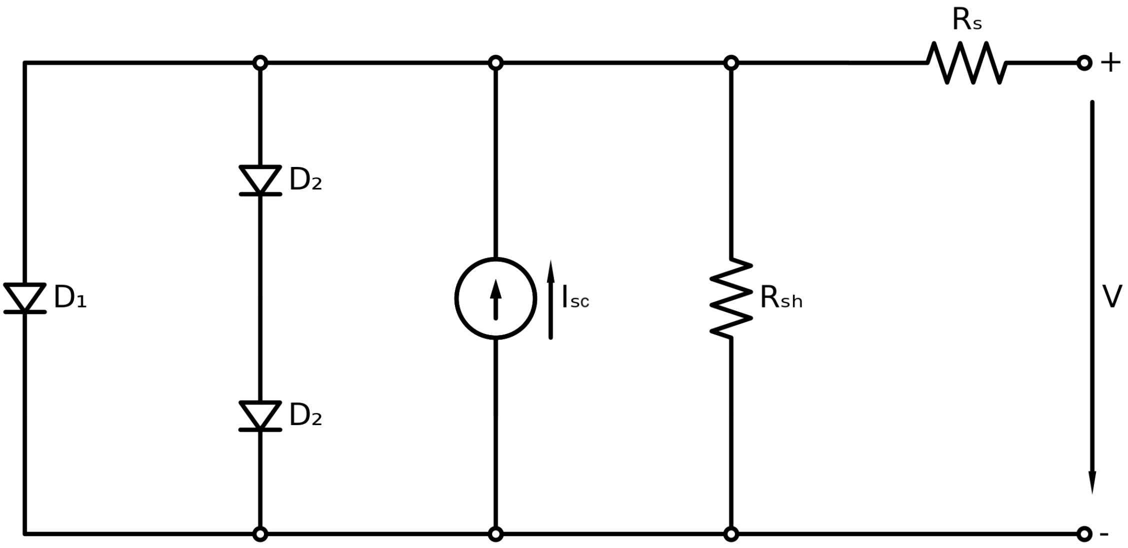

Figure 2.4: Two-Diode Model for a solar cell, where D_1 and D_2 represent recombination processes, R_{sh} the shunt resistance due to defects, and R_s the series resistance within the cell. Adapted from [23].

The diodes on the left describe direct (D_1 diode) or impurity (D_2 diodes) recombination effects. The resistor R_{sh} represents the shunt resistance of the solar cell, which mainly occurs due to pinholes in the absorbing material or at grain boundaries. R_s represents the series resistance that originates from transport resistances within the solar cell itself and the connection to the load. Considering this model, the IV-characteristic can be described by Equation 2.3 [23]:

$$\begin{aligned} I_Q = I_{s1}\left[\exp\left(\frac{e(V-I_QR_s)}{k_BT}\right)-1\right] + I_{s2}\left[\exp\left(\frac{e(V-I_QR_s)}{2k_BT}\right)-1\right] \\ + \frac{V-I_QR_s}{R_sh} + I_{sc} \end{aligned} \tag{2.3}$$

From Equation 2.3 the IV-Curve of a solar cell can be received with exemplary values as illustrated in the blue curve in Figure 2.5. The red curve represents the power output, where the current and voltage are multiplied. From both curves, the most important characteristics of a solar cell can be defined:

Short-circuit current density (J_{sc}) occurs when the positive and negative electrodes of a solar cell are directly connected with each other. This means that the voltage is zero [26]. It is the maximum current the solar cell can produce under the specific light source it is operating at this time.

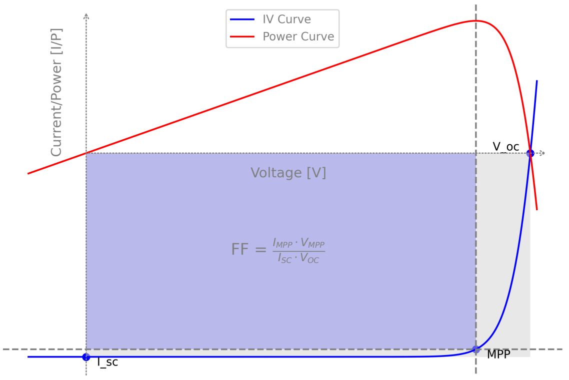

Figure 2.5: IV-Curve with corresponding Power Output Curve. Adapted from [26]

.

Open-circuit voltage (V_{oc}) is the maximum voltage a solar cell can provide to an external circuit. It only occurs when the cell is not connected to any load and the current is zero [26].

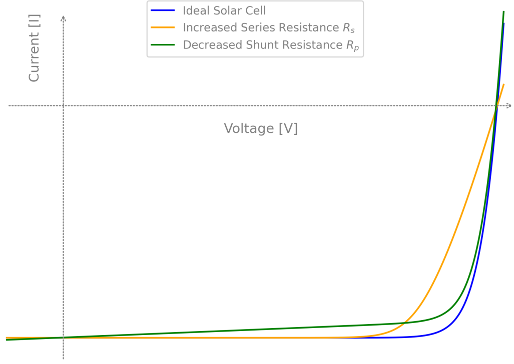

Figure 2.6: Influence of Series and Shunt Resistance on the IV-Curve. Adapted from [23]

.

Maximum Power Point (MPP) is the optimal operational point of the solar cell, where the power output is maximized. The power output of the solar cell is the product of current and voltage. The MPP is the maximum of the red curve in Figure 2.5 [26].

Fill factor (FF): The fill factor quantifies how close the solar cell's actual MPP is to its theoretical maximum, which is the product of V_{oc} and J_{sc}. In Figure 2.5, the necessary quantities are indicated in

the illustration, with the FF represented as the ratio of the blue rectangle to the grey rectangle area [26].
Figure 2.6 shows the result for varying R_p and R_s. It is notable, that both on their own as well as a combination affect the fill factor in a negative manner [23].

Based on these characteristics, the power conversion efficiency (PCE) can be defined. It describes how efficiently the solar cell can convert the incoming power of light into electrical power [26].

$$\mathrm{PCE} = \frac{P_{\mathrm{out}}}{P_{\mathrm{in}}} = \frac{V_{\mathrm{oc}} \times J_{\mathrm{sc}} \times FF}{P_{\mathrm{in}}} \tag{2.4}$$

where PCE is the power conversion efficiency, P_{out} is the output electrical power, P_{in} is the input light power, and V_{oc}, J_{sc}, and FF are the open-circuit voltage, the short-circuit current density, and the fill factor, respectively.

2.4 Semi-Transparent Solar Cells

Designing semi-transparent solar cells is always a compromise between charge carrier generation and the transmission of light in a certain wavelength region. Figure 2.7 displays the absorption coefficients of inorganic silicon and selected organic materials.

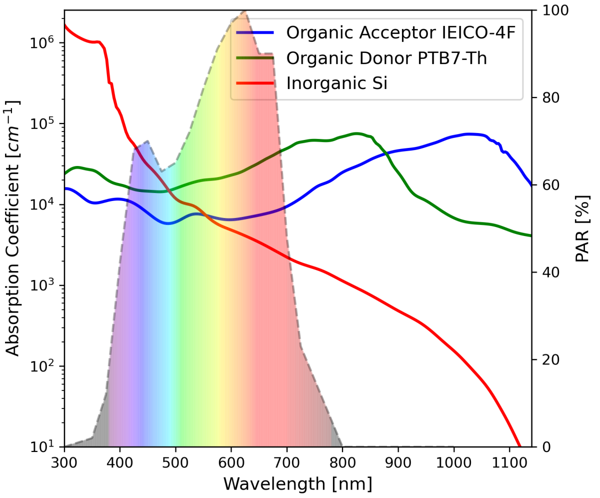

Figure 2.7: Absorption coefficients of inorganic Si and organic semiconductors. Organic materials have a stronger absorption in the infrared region compared to Si. The data has been adapted and modified from [29], [30].

Inorganic materials begin to absorb photons with a certain probability once the photon energy exceeds the bandgap (for silicon, this is indicated by the sharp drop around 1100 nm). As a result, photons in the visible range between 400 nm and 700 nm are absorbed. To achieve transparency, cleared areas between the active material must be

created.
In contrast, organic materials offer the ability to tune their absorption properties to mainly absorb in the infrared region while transmitting the visible light, making the active area itself semi-transparent [31].

To optimize solar cells for transparency, it is important to define a measurable quantity to compare different cells.
In the context of semitransparent organic solar cells, optimized for visual transparency as perceived by the human eye, the Average Visible Transmittance (AVT) is widely adopted. AVT is defined as the weighted average of the transmission spectrum of the solar cell, considering the spectral sensitivity of the human eye under standard AM 1.5G conditions. This is mathematically expressed by the following equation [12], [32]:

$$AVT = \frac{\int T(\lambda) \cdot V(\lambda) \cdot AM1.5G(\lambda)\, d\lambda}{\int V(\lambda) \cdot AM1.5G(\lambda)\, d\lambda} \tag{2.5}$$

where $T(\lambda)$ is the transmission spectrum of the solar cell, $V(\lambda)$ is the photopic response of the human eye, and $AM1.5G(\lambda)$ is the spectral distribution of sunlight under AM 1.5G conditions.

Another quantity that is commonly used for semitransparent applications, especially to better compare solar cells with different AVT values, is the Light Utilization Efficiency (LUE). The LUE combines the average visible transmittance with the power conversion efficiency of the device. It is defined as the product of AVT and PCE [12]:

$$\mathrm{LUE} = \mathrm{AVT} \cdot \mathrm{PCE} \tag{2.6}$$

In agrivoltaic applications, a well-established metric is not yet available. However, some papers propose a growth factor similar to the AVT by replacing the photopic response of the human eye with the response spectrum of plants (Photosynthetically Active Radiation, PAR). The growth factor (G) can be defined as follows [18], [33]:

$$G = \frac{\int T(\lambda) \cdot \mathrm{PAR}(\lambda) \cdot AM1.5G(\lambda)\, d\lambda}{\int \mathrm{PAR}(\lambda) \cdot AM1.5G(\lambda)\, d\lambda} \tag{2.7}$$

where $T(\lambda)$ and $AM1.5G(\lambda)$ are defined in the same manner as for the AVT, and PAR(λ) is the photopic response of the plants.

Figure 2.8 displays the AM 1.5G and PAR spectrum. The PAR spectrum is normalized between zero and one and can be seen as a weight for the light wavelengths that plants use for photosynthesis. This spectrum varies for each type of plant and the stage of the growing phase. Generally, plants have in common, that red light (around 660 nm) is more important in the later and blue light (around 450 nm) during the early phases of growth [34].
The exact PAR spectrum used in this work was developed by K. J. McCree. In his study he measured the action spectrum, absorptance, and quantum yield of photosynthesis across 22 different crop species, under specific wavelength ranges and in different growth phases. For this thesis, the average PAR spectrum derived from these 22 species was used in the growth factor calculation as seen in Equation 2.7 [34].

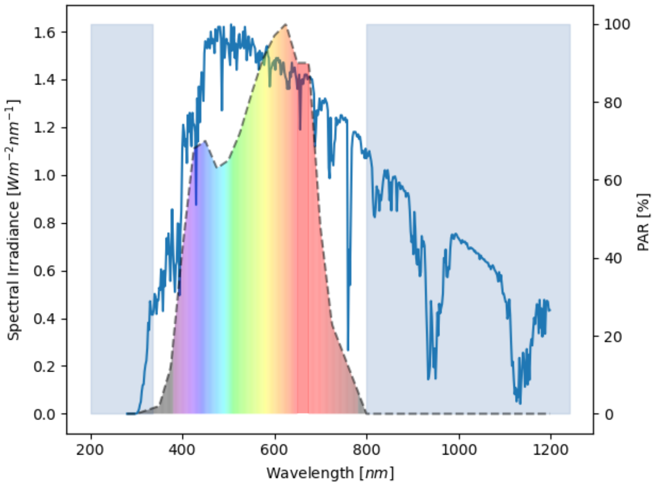

Figure 2.8: Spectral irradiance (blue curve) of the AM 1.5G and PAR spectrum (dashed curve).

2.4.1 Theoretical Limitation of Semi-Transparent Organic Solar Cells

Given that the goal of this thesis is to achieve a growth factor transparency greater than 60 %, it is important to discuss the theoretical efficiency limit of such cells. Naturally high transparency means that an important part of the solar spectrum is not used to generate electricity.
The Shockley-Queisser-limit determines the ideal theoretical efficiency for opaque solar cells based on the bandgap. Using the AM 1.5G solar spectrum, the maximum PCE for a single pn-junction inorganic solar cell with a bandgap of 1.34 eV is 33.7 % [23], [24].

Using multiple cells with different bandgaps on top of each other can increase this limit further. For example two stacked cells can increase it to 42 %, three to 49 % and an infinite number of cells to 68 % under unconcentrated sunlight [24], [35].

For single-junction semi-transparent organic solar cells, as developed in this thesis, a theoretical PCE limit can also be determined. For an ideal absorbing material, that transmits all visible light between 400 nm and 700 nm, the optimal Shockley-Queisser bandgap is estimated to be 1.12 eV. Considering further an external quantum efficiency outside the visible range of 100 %, the maximum theoretical power conversion efficiency for ST-OSC is 20.6 % [36].

As described in the beginning of Section 2.4, inorganic semiconductors would not be able to achieve this, as their transparency is provided by having gaps between the cell areas. This means that the PCE would be 0 % at 100 % transparency since no active area would remain.

Currently most organic materials partially absorb visible light. Therefore it is important to model their optical behaviour to determine the best layer thicknesses and configurations for an optimal performance. It also means that there is always a trade-of between transparency and power conversion efficiency.

Chapter 3

Photovoltaics in Agriculture

As the climate change affects agriculture significantly it becomes relevant to protect the cultivation of plants. Especially in areas that are affected by shortages of water, this can help to mitigate the effects of evaporating water [37]. Additionally, these systems can be combined with electricity production in terms of solar photovoltaic. This combination of agriculture and energy production is called agrivoltiac and can also reduce water evaporation [38].

Countries like for example the Netherlands that have big issues with space, can benefit further from this efficient land use.
The following section aims to clarify the requirements for semitransparent solar cells when used for agrivoltaic applications.

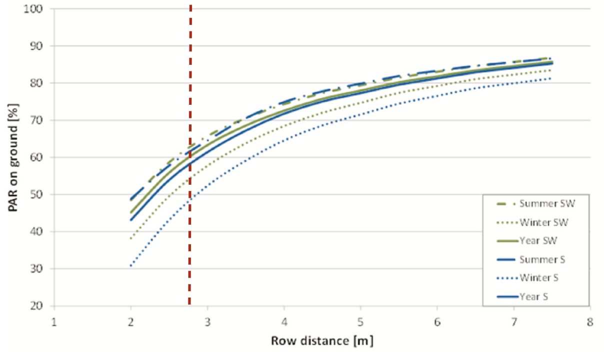

Figure 3.1: Percentage of global horizontal radiation on ground as a function of row distance, showing seasonal variations. At a row distance of 2.8 meters, maximum radiation reaches approximately 62 % during summer. Retrieved from [39].

Currently, most of these systems use classical silicon-based photovoltaic systems, that are not transparent within the visible range. Usually, the needed transmittance for the plants is achieved by including geometric aspects, meaning that the distance between the modules or cells is chosen in a way, that it transmits enough light for sufficient plant growth. Depending on the plant type, they can benefit from such shading or not. Trommsdorff et al. classify the crops based on their response to shading into three categories:

PLUS (potato), ZERO (celeriac, clover grass) to MINUS (winter wheat) [39].

Figure 3.1 shows the percentage of global horizontal radiation from the sun that reaches the ground level, based on the chosen row distance between the modules. The authors selected a row distance of 2.8 meters, which results in a maximum ground-level radiation of approximately 62 %.

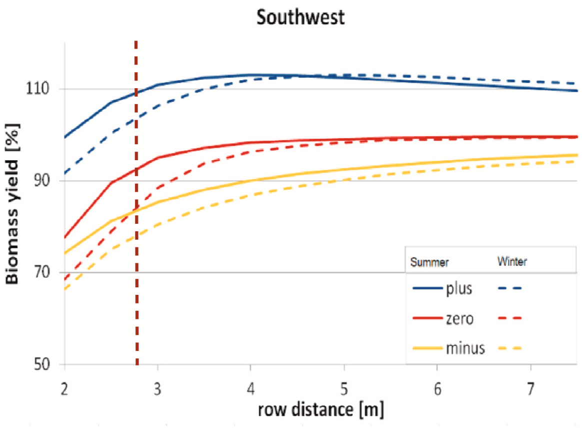

Figure 3.2: Biomass yield as a function of row distance and plant type (plus, zero, minus) for summer and winter. For a row distance of 2.8 meters the yields exceed 80 % of the baseline except for plants in minus category during winter. Retrieved from [39].

Figure 3.2 illustrates the expected yield based on plant type and row distance. For the chosen row distance of 2.8 meters, the expected yield is typically above 80 % of the yield without a photovoltaic (PV) system, except for MINUS plants during winter. This yield aligns with the expectations of local farmers, gathered through interviews, and meets the official regulations in Japan, where only agrivoltaic systems with an expected crop yield above 80 % gain public support [39]. The paper "Designing plant transparent agrivoltaics" suggests similar numbers for certain types of plants. For example, for basil and petunia the quality responses were saturated for 35 - 40 % shading (60 – 65 % G). On the other hand, tomatoes need a higher transparency of > 65 % [18].

Combining the results of these papers the minimum goal for G is 60 %. This might not be suitable for all types but for a variety of plants.

A second limiting factor for agrivoltaics is the high installation cost, due to the higher elevation, compared to regular open field photovoltaics [40]. As OSC are a lot more lightweight, it can be expected that these costs can be reduced as well.

Chapter 4

Optical Modelling of Thin Films

As solar cells convert light to an electrical current it is important to understand the nature of light and how it behaves, especially in thin films that are used in organic photovoltaics.

Optical modelling is a tool, that can calculate the solar cell's optical properties based on the material's optical characteristics, specifically the refractive index (n) and extinction coefficient (k). These optical properties are derived from the reflection, transmission and absorption (RTA) spectra of the individual layer materials. By utilizing the wave nature of light, it is possible to use interferences to increase the absorption without increasing the absorber thickness. Especially for semi-transparent organic solar cells this is important as it provides the opportunity to increase the transparency to a certain extend without reducing J_{sc}. Optical modelling makes it possible to estimate the needed layer thicknesses to find an optimum without doing an experiment each time. This chapter should provide an introduction to the basic principles of light and how these models can be used to predict and optimize the experimental results for ST-OSC.

4.1 Behavior of Light in Thin Films

Today, light is commonly described either as photons or as waves. Since the coherence length for solar light is about 1 µm and the layer thicknesses in organic photovoltaics are usually below this coherence length, the wave-like behavior of light is dominant and related models describe the behavior in thin film optical modelling the best. To define the behavior of light at a specific spatial position, it can be described as electromagnetic waves that are characterized by the electric field $\mathbf{E}(t)$, the magnetic field $\mathbf{H}(t)$, and the propagation direction of the wave. The vectors for $\mathbf{E}(t)$, $\mathbf{H}(t)$, and the wave's propagation direction are perpendicular to each other

[41].

To describe the behavior of the electric and magnetic fields one should start with the Maxwell's equations that are defined as the following [41]:

$$\nabla \cdot \mathbf{E} = \frac{\rho}{\varepsilon} \tag{4.1}$$

$$\nabla \cdot \mathbf{B} = 0 \tag{4.2}$$

$$\nabla \times \mathbf{E} = -\frac{\partial \mathbf{B}}{\partial t} \tag{4.3}$$

$$\nabla \times \mathbf{B} = \mu \mathbf{J} + \mu\varepsilon \frac{\partial \mathbf{E}}{\partial t} \tag{4.4}$$

Based on these equations it is possible to derive the wave equations for the electric and magnetic fields that describe light propagation in a vacuum [42]:

$$\nabla^2 \mathbf{E} = \mu_0 \varepsilon_0 \frac{\partial^2 \mathbf{E}}{\partial t^2} \tag{4.5}$$

$$\nabla^2 \mathbf{B} = \mu_0 \varepsilon_0 \frac{\partial^2 \mathbf{B}}{\partial t^2} \tag{4.6}$$

A common solution to this wave equation is a plane wave, in the form of [43]:

$$\mathbf{E}(\mathbf{r}, t) = \mathbf{E}_0 e^{i(\mathbf{k} \cdot \mathbf{r} - \omega t)} \tag{4.7}$$

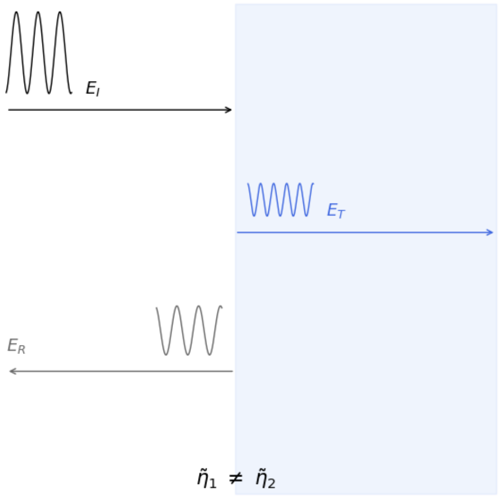

Figure 4.1: Light reflection and transmission at the interface between two materials with different refractive indices.

In thin film photovoltaics, it is especially important how the light behaves at the interface between two layers. When an electromagnetic wave encounters such interfaces as shown in Figure 4.1, one part of the wave is reflected back into the first material, and a second part is transmitted into the second material. The boundary conditions at these interfaces require that the tangential components of the electric and magnetic fields must be continuous. Further if considered, that there are no surface charges or currents, the normal components of the electric displacement field and the magnetic field must also be continuous. The following Fresnel equations describe the reflection and transmission coefficients at the interface, that are essentially the fractions of the reflected and transmitted with the incoming wave. These differ for s-polarized (perpendicular) and p-polarized (parallel) light [43].

For s-polarized light, where the electric field is perpendicular to the plane of incidence, the Fresnel reflection and transmission coefficients are given by [43]:

$$r_s = \frac{n_1 \cos\theta_i - n_2 \cos\theta_t}{n_1 \cos\theta_i + n_2 \cos\theta_t} \tag{4.8}$$

$$t_s = \frac{2n_1 \cos\theta_i}{n_1 \cos\theta_i + n_2 \cos\theta_t} \tag{4.9}$$

For p-polarized light, where the electric field is parallel to the plane of incidence, the corresponding Fresnel coefficients are [43]:

$$r_p = \frac{n_2 \cos\theta_i - n_1 \cos\theta_t}{n_2 \cos\theta_i + n_1 \cos\theta_t} \tag{4.10}$$

$$t_p = \frac{2n_1 \cos\theta_i}{n_2 \cos\theta_i + n_1 \cos\theta_t} \tag{4.11}$$

The angles of incidence (θ_i) and transmission (θ_t) are related by Snell's Law [43]:

$$n_1 \sin\theta_i = n_2 \sin\theta_t \tag{4.12}$$

These expressions assume real refractive indices. When considering materials with absorption, the refractive index becomes complex n $\rightarrow \tilde{\eta}$, and the Fresnel coefficients must be modified accordingly [43].

For multi-layer stacks, as seen in Figure 4.2, the waves on an interface become even more complicated, as the reflected waves from subsequent interfaces in the stack also affect the waves at the first interface. There are several methods solving this issue, one of them that is computationally less expensive is the transfer matrix method (TMM), that will be explained in the next section. This method is also used in the commercial software Scout and the python script that where both used for the optical modelling of the solar cells in this thesis.

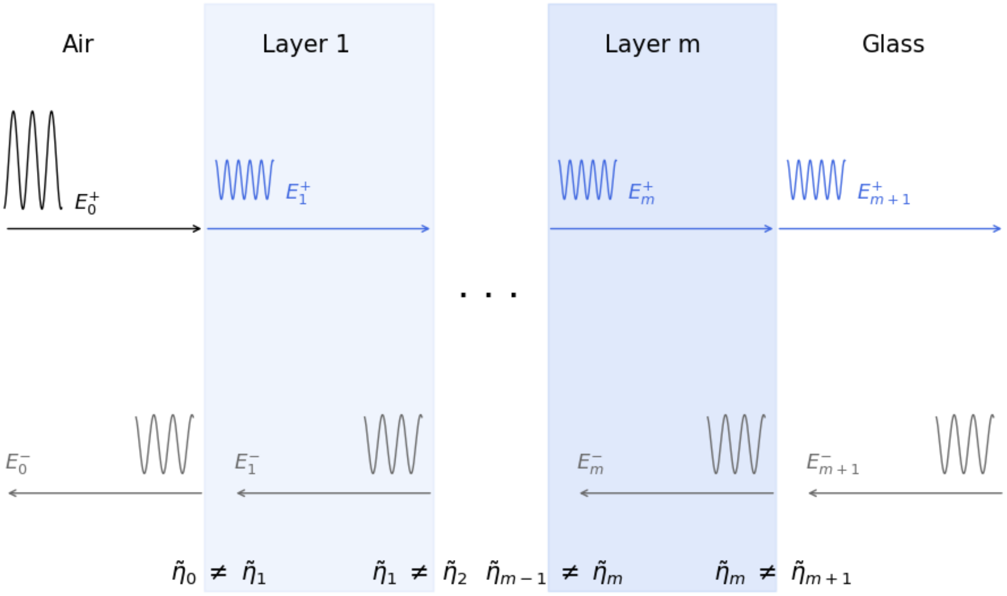

Figure 4.2: System of interfaces showing the complexity of wave interactions in multi-layer stacks, as found in OSC. Adapted from [44].

4.2 Light in Multiple Layer Stacks - Transfer Matrix Method

The organic solar cell is modeled as a series of multiple thin layers as seen in Figure 4.2, that are stacked between air and a glass substrate. Each of the layers has a different refractive index and thickness. To consider the effect of subsequent layers another reflected wave can be assumed for each interface encountering it from the right [44].

In the TMM model, the behavior of light at an interface is described by an interface matrix M. For perpendicular incidence, the interface matrix between layers j and $j+1$ is given by:

$$M_{j,j+1} = \begin{pmatrix} \frac{\tilde{\eta}_j + \tilde{\eta}_{j+1}}{2\tilde{\eta}_j} & \frac{\tilde{\eta}_j - \tilde{\eta}_{j+1}}{2\tilde{\eta}_j} \\ \frac{\tilde{\eta}_j - \tilde{\eta}_{j+1}}{2\tilde{\eta}_j} & \frac{\tilde{\eta}_j + \tilde{\eta}_{j+1}}{2\tilde{\eta}_j} \end{pmatrix} \tag{4.13}$$

where $\tilde{\eta}_j$ and $\tilde{\eta}_{j+1}$ are the complex refractive indices of the j-th and $(j+1)$-th layers [44].

Once the light surpassed the interface it propagates through that layer. Which can be described by a layer propagation matrix P [44]:

$$P_j = \begin{pmatrix} e^{-ik_jd_j} & 0 \\ 0 & e^{ik_jd_j} \end{pmatrix} \tag{4.14}$$

where $k_j = \frac{2\pi\tilde{\eta}_j}{\lambda}$ is the wave vector in the j-th layer, d_j is the thickness of the j-th layer, and λ is the wavelength of light [44].

To describe the overall transfer matrix M for the entire multilayer stack the propagation and interface matrices of the individual layers have to be multiplied in the same sequence as the layers are ordered in the stack [44]:

$$M = M_{m,m+1}P_m \dots M_{1,2}P_1M_{0,1} \tag{4.15}$$

This combined matrix relates the electric fields at the front and back of the structure in the following way [44]:

$$\begin{pmatrix} E_0^+ \\ E_0^- \end{pmatrix} = M \begin{pmatrix} E_{m+1}^+ \\ E_{m+1}^- \end{pmatrix} \tag{4.16}$$

If no reflection at the back substrate ($E_{m+1}^- = 0$) is assumed, the reflection (R) and transmission (T) coefficients can be written as [44]:

$$R = \frac{M_{21}}{M_{11}} \tag{4.17}$$

$$T = \frac{1}{M_{11}} \tag{4.18}$$

As seen in the equations before, the coefficients are wavelength dependent, meaning that they are spectra. Based on those spectra, the AVT and G can be calculated as described in Section 2.4.

Similarly, it is also possible to calculate the absorption within the absorber layer and therefore get an estimate of the maximum achievable current $J_{Gen,max}$. For a comprehensive explanation of this approach refer to the work by Md. Shofiqul Islam titled ”In-Depth Analysis of Organic Solar Cells Using Transport Equation and Optical Transfer Matrix Method with Detailed Analytical Derivations” [44].

Chapter 5

Fabrication and Characterization of Solar Cells

To achieve the desired result of the thesis, several iterations of simulating and building solar cells were conducted. The following chapter describes details about the methods and materials used, as well as potential errors that might occur during the solar cell fabrication process.
Generally speaking the fabrication can be split into three main steps. First, a semi-transparent back electrode is sputtered onto glass substrates. Next, the organic absorber and charge transport materials are spin-coated onto these sputtered electrodes. These coated layers have to be cleaned off from the contact pads of the sputtered back electrode in order to receive a working solar cell. Finally, a support structure composed of chromium and silver is evaporated onto the substrate. This support structure links HTL, which also functions as the top electrode, to the edges of the substrate, providing another terminal to connect the cell. These cells are then characterized in terms of their optical and electrical properties, which provides valuable information for future experiments.

5.1 Sputtering of the Back Electrode

In order to sputter the back electrode onto a glass substrate, any dust or organic residues has to be removed first. Therefore the glass substrates are placed in containers filled with acetone, isopropanol, and deionized water while subjected to ultrasonic cleaning in several runs.

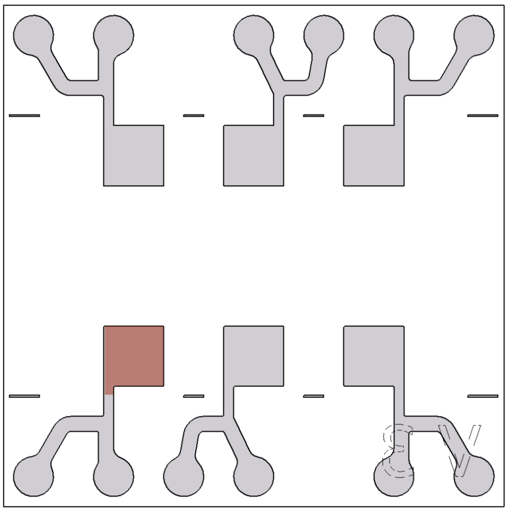

Figure 5.1: Substrate structure, which accommodates six solar cells, used for the sputtering process. The active area of each cell ($9.25\,\mathrm{mm}^2$) is marked in red in one of them.

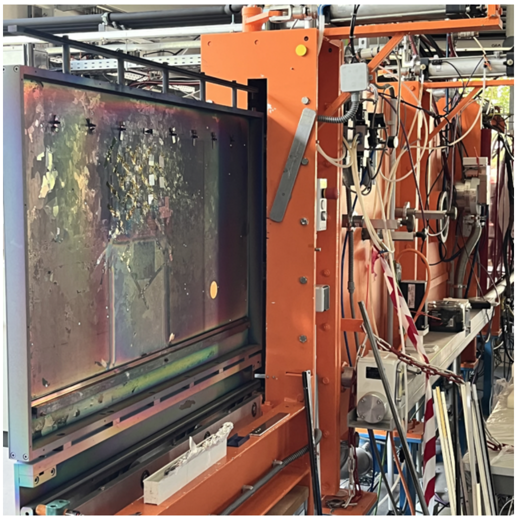

Figure 5.2: Picture of the sputtering process, displaying the equipment used to deposit the layers of the back electrode on the glass substrate.

After being dried with a nitrogen gun, the substrates were stored in containers and sealed with tape for the transportation to the sputtering location. Handling of the substrates while being placed in the mask for the sputtering process was conducted under a fume hood to minimize dust contamination.
A metal mask was used to pattern the structure on the substrate during the sputtering process, as illustrated in Figure 5.1. The entire sample is referred to as the substrate, with each subunit termed a cell. Each substrate accommodates six solar cells. The sputtering of the layers was done on the machine displayed in Figure 5.2 by Martin Mattenheimer.

The back electrode used for this thesis consists of a thin silver layer to ensure sufficient conductivity and several layers of metal oxides to adjust the optical properties of the back electrode.

5.2 Spin-Coating of Charge Transport and Absorber Layers

The next process involves the spin-coating of the charge selective ETL and HTL layers, as well as the absorber material. The absorber material is a blend of electron-donating polymers and electron-accepting small molecules or fullerene derivatives, commonly referred to as a ”blend”.
The three layers can be arranged in two ways, either ETL-Blend-HTL or HTL-Blend-ETL, which defines the polarity of the bottom and top electrode. As the last sputtered aluminum doped zinc oxide (AZO) layer from the previous building step aligns well energetically to function as an ETL, the first configuration was chosen for this work. But as previous studies, with a similar arrangement of the sputtered back electrode showed an increased occurrence of shunts an additional zinc oxide (ZnO) layer was coated to smooth the surface and function as an additional electron transport layer.

Next, several absorber materials were tested, based on results reported in other literature or promises of the producer, which indicated high absorption primarily in the infrared range. Additionally, the high-performance blend PV-X Plus (PV2300:PV-A-3:N1100 1:1:0.2 from Raynergy Tek) was used. Although it is not optimized for semitransparency, this blend was stable in very thin layers and was then able to provide decent transmissions.

Figure 5.3: Spin coater used for depositing the charge selective layers HTL and ETL, as well as the absorber layer.

The hole transport layer consisted of two different materials. Initially, a thin layer of HTL-X (a PEDOT-based HTL purchased from Raynergy Tek) was applied. While its energetic alignment matched the donor materials, its con-

ductivity is insufficient. Thus, it was
applied very thinly (around 30 nm) and followed by a second, more conductive layer of SCA2003 (purchased from Heraeus). The ZnO, absorber materials and HTL materials could be processed from solution using solvents such as o-xylene, ethanol, and isopropyl alcohol.

The layers were deposited using a spin-coater as shown in Figure 5.3, that rotates the substrate for a preset time and speed. When a droplet of the material is placed onto the substrate, the centripetal forces distribute the material, which results in a very uniform thin film. The droplet can be placed either before (drop-spin) or when the rotation (spin-drop) is already started.
To reach the desired thicknesses the materials were coated with several spin-coating speeds on glass substrates beforehand and measured as will be explained in Section 5.4.3. With a logarithmic fit an estimate about the needed spin-coating speed for a desired thickness can be calculated. The samples were dried on a hotplate (annealing) in-between different spin coating steps or in the end, to allow the solvent to evaporate.

Table 5.1: Spin-coating and thermal annealing procedure for the different materials used for the experiments.

Material	**Concentration**	**Volume [µL]**	**Spin-speed [rpm]**	**Spin-duration [s]**	**Annealing temp. [°C]**	**Annealing time [min]**
ZnO	1-2.5 wt%	100	4200	60	110	10-27
PV-X Plus	15-22 [mg/ml]	80	2000-4700	60	110	10-17
HTL-X	-	80	3000-5100	60	110	7-10
SCA2003	-	250	3500-5000	60	110	5-10

Unless otherwise stated, the blend was coated at 60 °C, and all other materials at room temperature. As the temperature inside the glove box can not be controlled precisely, the temperature was varying between 25 °C and 35 °C .
More details on the spin coating parameters are given in Table 5.1.

To connect the cells to the measuring mask, the spin-coated layers have to be removed from the contact pads. The two HTL layers have been removed first from the contacts with a tape, alongside the dotted line shown in Figure 5.1. Then the blend was removed from the contact pads using a wiping pad soaked with o-xylene. To prevent the HTL from contacting the bottom electrode and thus to reduce the risk of shunting, there was a gap left between the taping (1) and wiping edge (2). The cell area is restricted by the taping edge. The final results of both steps can be seen in Figure 5.4.

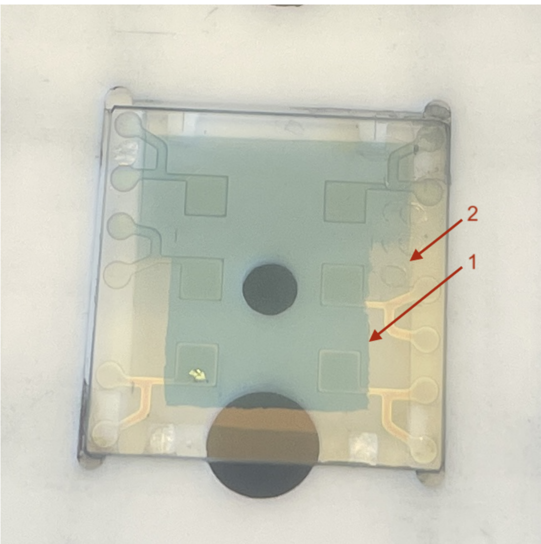

Figure 5.4: Substrate image after the wiping process. (1) Indicates the edge after the removal of the two HTL layers, and (2) shows the edge after the additional wiping of the contact pads.

5.3 Evaporation of the Support Structure

As a final step a support structure, that connects the cells to the pins of the measuring mask, has to be evaporated onto the substrates.

It is common to use an additional metal grid on top of the cell area to improve the conductivity when the HTL layer is not able to meet performance demands. On the other hand, this grid causes shading, which reduces the amount of light reaching the cell and decreases the J_{sc}. Additionally, such metal grids reduce the overall transparency, proportional to the area they cover. With the available evaporation masks this would account for a 10 % loss in growth factor. As the conductivity of the SCA2003 layer is comparably high and the generated J_{sc} is small for such thin absorber layers, only the support structure was evaporated.

Since evaporated silver does not stick well to glass, an additional layer of chromium is also evaporated. Therefore the support structure consists of approximately 5 nm of chromium and 100 nm of silver.

5.4 Characterization of Devices and Single Layers

To characterize solar cells for their fit in agrivoltaic applications it is important to consider their electrical and optical properties.

5.4.1 IV-Characteristics

To obtain the electrical characteristics the solar cells were tested using an AAA-class solar simulator (SP94063A from Newport) as a light source and an array of three Keithley Multimeters, that were able to measure the IV-Characteristics of three cells simultaneously.

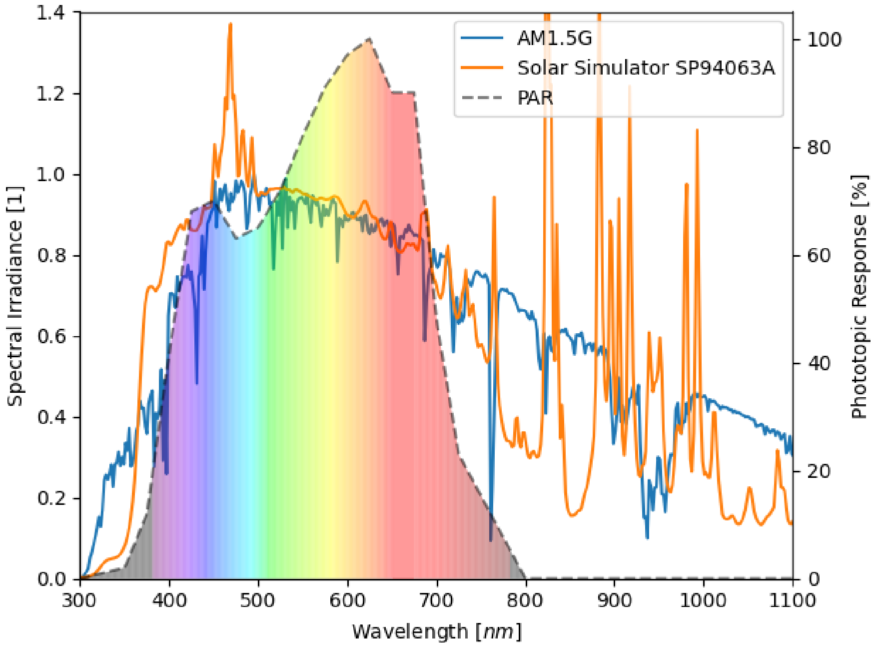

Figure 5.5: Spectral mismatch between the AM1.5G standard spectrum and the solar simulator SP94063A. The PAR spectrum is also shown in the background for reference.

Figure 5.5 shows that the spectrum of the solar simulator differs from that of the normalized AM 1.5G spectrum. To account for that mismatch a correction has to be calculated. To do so, the spectral response of a reference silicon solar cell $SR_{\text{ref}}(\lambda)$, the spectral response of the tested cell $SR_{\text{test}}(\lambda)$, the AM 1.5G spectrum

$E_{\mathrm{AM1.5G}}(\lambda)$ (obtained from a standard source) [45], and the spectrum of the solar simulator $E_{\mathrm{SoSi}}(\lambda)$ have to be measured.
Most of the data was available from earlier measurements of the working group but the spectral response measurement of the tested cell had to be conducted. This was done by Clemens Baretzky. As the process is time consuming and variations for similar stack structures are small, the measurement was only conducted once.
With these, the mismatch factor can then be calculated as:

$$M = \frac{\int E_{\mathrm{AM1.5G}}(\lambda) \cdot SR_{\mathrm{ref}}(\lambda)\, d\lambda}{\int E_{\mathrm{SoSi}}(\lambda) \cdot SR_{\mathrm{ref}}(\lambda)\, d\lambda} \cdot \frac{\int E_{\mathrm{SoSi}}(\lambda) \cdot SR_{\mathrm{test}}(\lambda)\, d\lambda}{\int E_{\mathrm{AM1.5G}}(\lambda) \cdot SR_{\mathrm{test}}(\lambda)\, d\lambda} \tag{5.1}$$

The $\mathrm{J_{sc}}$ under the solar simulator should match that under the AM 1.5G illumination:

$$J_{sc,\mathrm{test,SoSi}} = J_{sc,\mathrm{test,AM1.5G}} \tag{5.2}$$

Therefore, Equation 5.1 can be simplified to:

$$J_{sc,\mathrm{ref,SoSi}} = \frac{J_{sc,\mathrm{ref,AM1.5G}}}{M} \tag{5.3}$$

For each IV measurement the intensity of the solar simulator had to be adjusted to match the current of the reference cell, so that the $\mathrm{J_{sc}}$ of the measured cell represents the current under AM 1.5G conditions. The IV measurement is conducted by placing the substrates in a measuring mask, where each cell is contacted at the back and top electrode. The mask is then placed on the solar simulator and an external voltage between −1 V to 1 V is applied. The resulting current at each voltage point is then measured. In that way the relationship between voltage and current is captured and forms the IV-curve. As explained in Section 2.3 this IV-curve provides information about the solar cell's performance, in form of the open-circuit voltage ($\mathrm{V_{oc}}$), short-circuit current ($\mathrm{J_{sc}}$), fill factor (FF), and efficiency (PCE). Applying a negative bias is essential to understand potential issues, as it helps measure leakage currents and reveals the shape of the IV-curve more clearly, which can provide insights into increased shunt or series resistance. After the measurement under illumination, the procedure is repeated in the dark. For this, the cells are covered with a black fabric, and all lights are turned off. The behavior in the resulting "dark curve" can offer additional information about recombination effects.

5.4.2 Optical Properties

The reflection and transmission spectra of individual layers and full solar cell stacks were measured using a UV-VIS-NIR spectrometer (LAMBDA 950 from Perkin-Elmer). The device is equipped with an integrating sphere, allowing the calculation of absorption A from the measured reflection R and transmission T ($A = 1 - R - T$). Based on these results, the refractive index n and extinction coefficient k values can be estimated for individual layers on glass. For the full solar cell stack, the AVT and growth factor values can be calculated.

5.4.3 Physical Properties

Further it is important to measure the thickness of individual material layers for specific concentrations and spin coating speeds in order to reach the targeted thicknesses efficiently and to estimate correct n and k values for the simulations.
The thicknesses were measured using a Veeco Dektak 150 surface profilometer.

5.5 Optical Modelling and Short Circuit Current Density Prediction

From the RTA data and the thickness of a film, the n, k values of the material were fitted using the software Scout. To design the electrodes, the data from my predecessors Leonie Pap and Bertolt Schirmacher was used.
The n, k values of each material were then used to simulate the optical behavior either using the software Scout or a python-based transfer matrix approach. In the Python script the module "tmm" by Steve Byrnes was used to simulate the amplitude distribution of the light throughout the stack. The module also calculates the absorption within an individual layer. Both approaches, Scout or the Python script, were used simultaneously to ensure the same results in both methods. The Python script was especially necessary, as Scout did not allow to change the spectrum in the AVT calculation to the PAR spectrum in order to calculate the G. To estimate the J_{sc} of a device, every photon that is absorbed in the active material is counted as a generated electron-hole pair, meaning that the internal quantum efficiency (IQE)

of the solar cell would be at 100 % across all wavelengths. The sum of the absorbed photons then gives the J_{sc}:

$$J_{sc} = \sum_{\lambda} A(\lambda) \cdot E_{\mathrm{AM1.5G}}(\lambda) \cdot \Delta\lambda \tag{5.4}$$

with the fraction of light that is absorbed in the blend $A(\lambda)$, the reference spectrum of the sun $E_{\mathrm{AM1.5G}}(\lambda)$ that is in this case converted to #photons/$(m^2 \cdot nm$, and the distance between the discrete wavelength values $\Delta\lambda$.

This approach overestimates the J_{sc}, since the IQE is generally lowered by any loss mechanism.

The calculation of the AVT and G is done as described in Section 2.4, while the transmission spectrum is the absorption within an infinitely thick layer of air behind the stack.

To find optimal layer thicknesses within a given stack, the Python module SciPy was used. The thicknesses of some or all of the layers were given as parameters, and the function `scipy.minimize` was used to find a minimum for the value 1/(G), in order to reach the targeted G of above 60 %.

The simulations were used for several reasons. Based on the optical properties, an estimate of the effect of varying layer thicknesses can be calculated. Since certain effects can occur abruptly, it is important to change layers in the experiment one by one, starting from a stack that was functional. Otherwise, it would not be clear where the experiment went wrong. In this study, the entire layer stack was designed based on the results of my predecessor Bertolt Schirmacher and my supervisor, Leonie Pap. Their results were used as a starting point to design a new stack configuration that meets the growth factor target. The exact configurations for each experiment will be explained in the subsequent sections.

On the other hand, the simulations can also be used to compare the measured RTA spectra of the built devices to the simulation. The layer thicknesses can be fitted to match the measurements more closely, providing an estimate of how well the desired layer thicknesses were experimentally replicated.

5.6 Error Sources and Limitations during Fabrication

Several potential sources of error, that can occur during the fabrication process of the solar cells, were identified and are summarized here. Their influence on in-batch and batch-to-batch variations will be discussed in more detail in Section 6.

During both, the sputtering and spin-coating process it is important do avoid dust contamination, as it can lead to defects, causing the shunt resistance to decrease and thus reduce the performance of the cell. Furthermore several other factors, such as small variations in sputtering rate, coating conditions, or environmental factors like temperature fluctuations inside the glove box (between 25°C and 35°C)can influence the layer thickness and its optical properties. Additionally, the adhesive properties of materials in the stack differ from those on glass, which could lead to variations in layer thickness between the stack and the samples coated on glass. Since the later ones are used to estimate the n and k values for optical modeling, these discrepancies also impact the comparison between simulations and experiments. The thicknesses are measured using the Dektak profilometer, which has an accuracy of about 2 nm and cannot effectively measure thicknesses below 20 nm.
Some materials, like SCA2003, also showed variations in thickness across a single substrate, with the center being thicker than the edges.
Once the layers are coated, the exact cell area is determined by the accuracy of the manually applied taping edge as shown in Figure 5.4.
Finally, some variations occur during characterization due to slight differences in light intensity across the measurement positions of the solar simulator. Especially measurement position five has a slightly higher current.

Chapter 6

Results and Analysis

As described in Section 1.2, the goal of this thesis is to develop a solar cell with a growth factor above $G = 60\,\%$, in order to allow the use of solar cells in agricultural fields for energy generation while also maintaining a reasonable plant yield. In contrast to the main focus of the group, where the solar cells are optimized to reach a high light utilization efficiency aimed at the photopic response of the human eye, the focus of this work is to reach the growth factor target, with less focus on the power conversion efficiency.

The general concept, to achieve a solar cell with a meaningful efficiency, while simultaneously being transparent in the visible region of the solar spectrum is to absorb light mainly in the near infrared region, as it still provides about $52\,\%$ of the total energy coming from the sun [46]. Moreover, selective infrared reflection of the back electrode can be utilized to enhance cell performance. In principle, light that is not initially absorbed by the photoactive layer can be redirected back into the cell stack, thereby increasing the likelihood of absorption by the photoactive material. This process can contribute to improved current generation and thereby overall efficiency of the device [47]. This is commonly done by a thick bottom electrode often consisting of aluminium. But in the case of semi-transparent organic solar cells, the electrode also has to be highly transparent in the PAR region, making such a thick electrode unusable.

The development of such a semi-transparent organic solar cell can be split into several parts. Initially, a previously developed and well established cell stack within the group was evaluated under the new characteristic G in order to set a benchmark for the work within this thesis. Following this, multiple absorber materials were tested to evaluate their electrical and optical properties in order to select a blend that is suited best for the desired application. Afterwards, several electrodes were developed using optical modelling as described in Section 4.2 to maximize the transmission in the PAR spectrum and the light absorption in the absorber layer. They were then sputtered, to replicate the simulations experimentally. To demonstrate the potential of such a solar cell, the simulations were also done for a theoretical absorber, which only aborbs light in the desired region. Finally, the solar cell stack was optimized in several experiments for the blend PV-X Plus to reach the desired growth factor target of over 60 %.

During the time when the experiments were conducted, the light bulb in the sun simulator was replaced, but it was only later noticed that the new lamp had a slightly different spectrum. This means that the mismatch factor should have been recalculated in order to get consistent results between all experiments. It will be clearly addressed in the experiments when it is relevant. Thus, the focus within each experiment is on trends between the cells built in the same batch or under identical conditions, rather than on the absolute values of J_{sc} and PCE.

6.1 Benchmark

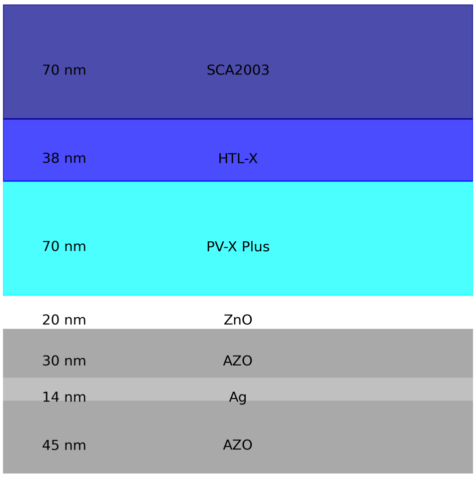

Figure 6.1: Full stack organic solar cell including the layer thickness for each individual layer commonly used in the working group. Representing the benchmark solar cell stack.

A semi-transparent cell stack that was previously used as a well established standard within the working group is shown in Figure 6.1. It consists of a sputtered electrode with a thin silver layer in between two AZO layers. The first AZO layer is for optical engineering and that the following silver layer adheres well. The second layer functions as the ETL layer and is also relevant for the optical engineering. Additionally, its thickness also affects how the active layer is positioned relative to the reflected light's intensity and therefore has an influence on the absorption within the active material and the short-circuit current.

The thickness of the silver layer influences both the transmittance and the electrode's conductivity. In this configuration, a thickness of 14 nm was found as an optimum for maximizing light utilization efficiency, as increasing the thickness enhances NIR reflection more rapidly than it reduces transparency. Based on previous results of the group, it is still not recommended to go below 12 nm, even for experiments where transparency is the primary focus, as it was not possible to sputter homogeneous layers. The PV-X Plus layer is positioned between AZO and HTL-X. They act as the ETL and HTL, to ensure proper energetic alignment and efficient charge transport to the electrodes. Additionally, the HTL-X also improves the adhesion of a second HTL layer using SCA2003, since it cannot be directly coated onto the blend. The SCA2003 layer also functions as the high-conductivity transparent top electrode.

The stack was characterized in terms of its electrical and optical properties. The results for the J_{sc}, V_{oc}, FF and PCE are shown as a figure of merit in Figure 6.2. Notably the $PCE_{median} = 8\,\%$.

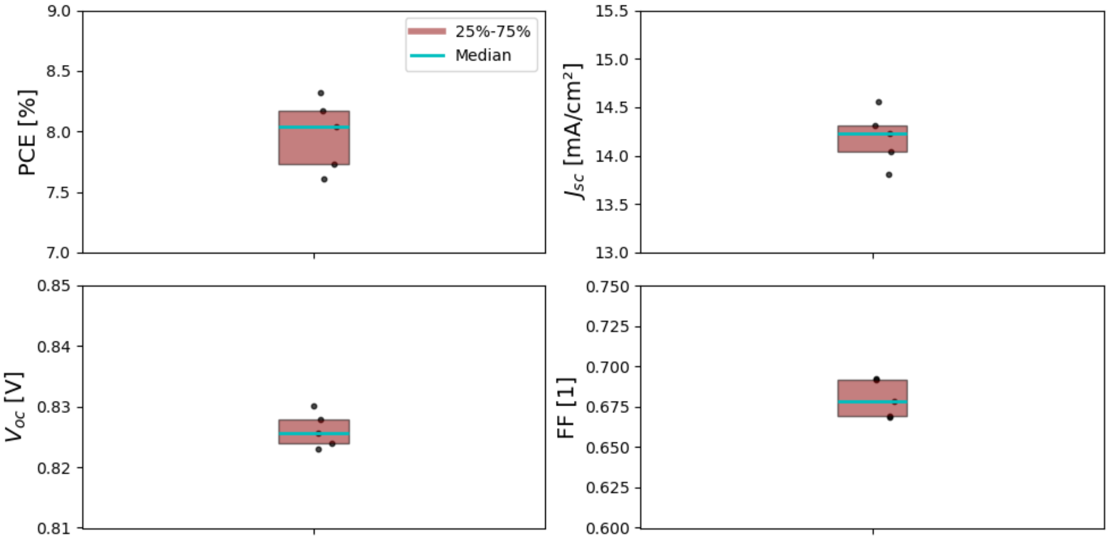

Figure 6.2: Measured characteristics for solar cells with single silver electrode.

The graph also provides an indication of the order of magnitude for variations within a batch or substrate. These variations are due to several reasons. For example, small differences in annealing time, often less than a minute, are common during the experimental process and can affect the material morphology. Contaminations, either within the material itself or as particles on the substrate, can also lead to

uneven layer thicknesses across the substrate.
Figure 6.2 shows that the spread in J_{sc} is more significant compared to the other parameters. It can be mainly attributed to slight differences in the cell area, as those are defined manually by the taping edge during the production process.
Finally, the measurement position within the measurement mask also affects the results. Especially position five tends to have a higher intensity than the others and was therefore avoided, when possible.

In terms of its optical properties, the configuration achieves a growth factor of $G = 39.7\,\%$.

6.2 Evaluation of Absorber Materials

As the transparency and efficiency of the cell is primarily restricted by the absorption of the photoactive material, several blends were evaluated in terms of their optical and electrical properties. These blends were chosen based on their expected low absorption in the visible range and high absorption in the NIR region, either recommended from other literature, comparable blends found in literature, or from the supplier company itself [48]–[51].

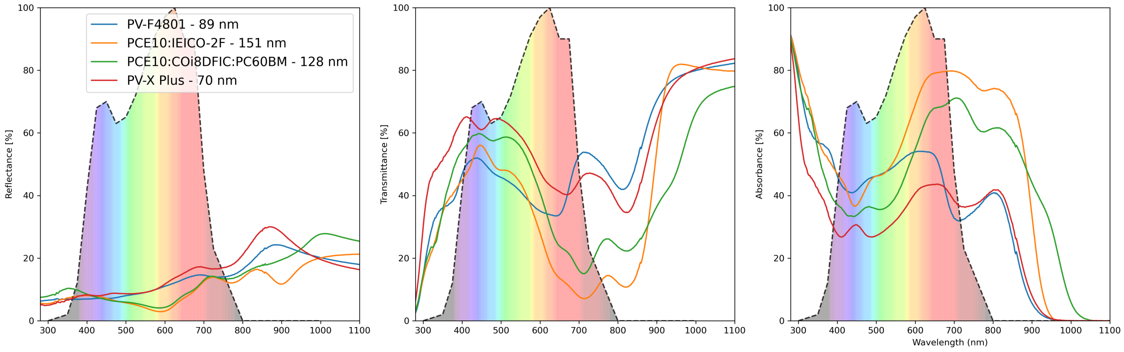

Figure 6.3: Measured RTA spectra for different absorber materials coated on glass. The graph indicates that PCE10:COi8DFIC:PC60BM and PCE10:IEICO-2F absorb stronger in the near infrared region compared to PV-X Plus or PV-F4801.

Figure 6.3 shows the absorption, reflection and transmission spectra with different layer thicknesses for each blend. The chosen thicknesses were selected to ensure that the materials form a coherent layer and remain electronically functional. Due to the different layer thicknesses, the absorption intensities cannot be directly compared and instead, the focus should be on the wavelength regions in which they absorb. In particular, the blends containing PCE10 absorb further into the infrared region, which is beneficial to capture more energy from the light spectrum. In contrast, PV-F4801 has the lowest optical performance compared to the other blends. Figure 6.4 shows the electrical properties of a stack with each of the materials. The desired layer thicknesses and stack is described in Table 6.1.

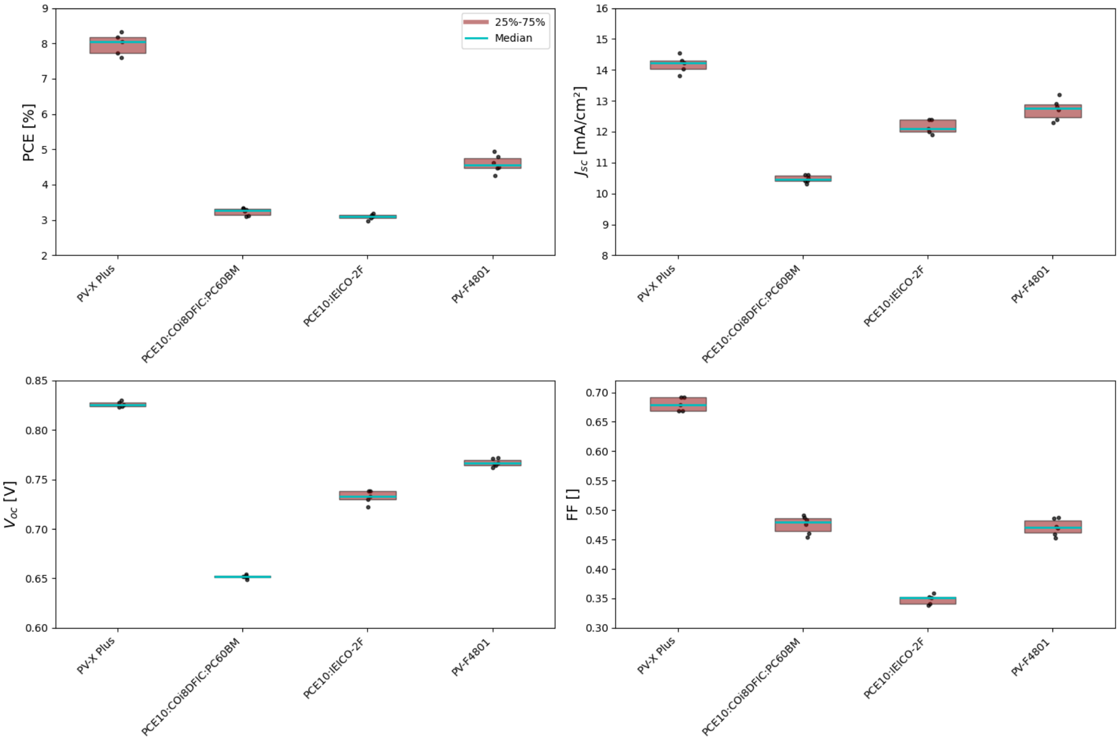

Figure 6.4: Measured characteristics for different absorber materials. Especially noticeable is the low FF for PCE10:COi8DFIC:PC60BM, PCE10:IEICO-2F and PV-F4801.

Table 6.1: Different stack layers and their corresponding thicknesses for each substrate.

Material	**PV-X Plus [nm]**	**PCE10:COi8DFIC-:PC60BM [nm]**	**PCE10:IEICO -2F [nm]**	**PV-F4801 [nm]**
AZO	45	45	45	45
Ag	14	14	14	14
AZO	30	40	40	40
ZnO	20	0	0	0
Blend	70	128	151	89
HTL-X	38	38	38	38
SCA2003	70	70	70	70

It is worth noting, that the layer thicknesses between each materials vary, as the initial test should only evaluate if a material is potentially suited for the desired application or not. Figure 6.4 shows that the blends PCE10:COi8DFIC:PC60BM, PCE10:IEICO-2F and PV-F4801 have a weak electrical performance, especially showing in a low V_{oc} and FF. PV-F4801 was additionally tested in other non-transparent stacks with different HTL and ETL configurations to see if the bad performance can be explained with a wrong energetic alignment, but no improvement was found. The biggest downside for all three materials is the low transparency, as shown by the low growth factor in Table 6.2, due to the thick layers needed while already having a low electrical performance. To remain competitive, the layers would need to be a lot thinner and thus absorption and cell performance would be reduced even further.

These findings show that PV-X Plus remains the most suitable candidate to achieve the targeted growth factor.

Table 6.2: Growth factor results based on simulations for the different absorber materials.

Material	PV-X Plus	PCE10:COi8DFIC-:PC60BM	PCE10:IEICO -2F	PV-F4801
G [%]	37.6	31.3	24.4	29.9

6.3 Stack Optimization for a Theoretical Absorber

To evaluate the performance of a ST-OSC stack, it is helpful to define the upper limit such a stack can achieve. For this purpose, a theoretical absorber material was defined with the n and k values shown in Figure 6.5. The extinction coefficient k was set to 1 in the wavelength regions where light should be absorbed and 0 where it should not. On the other hand, the refractive index n was chosen to have comparable values to that of a typical organic material, in this case, PV-X plus.

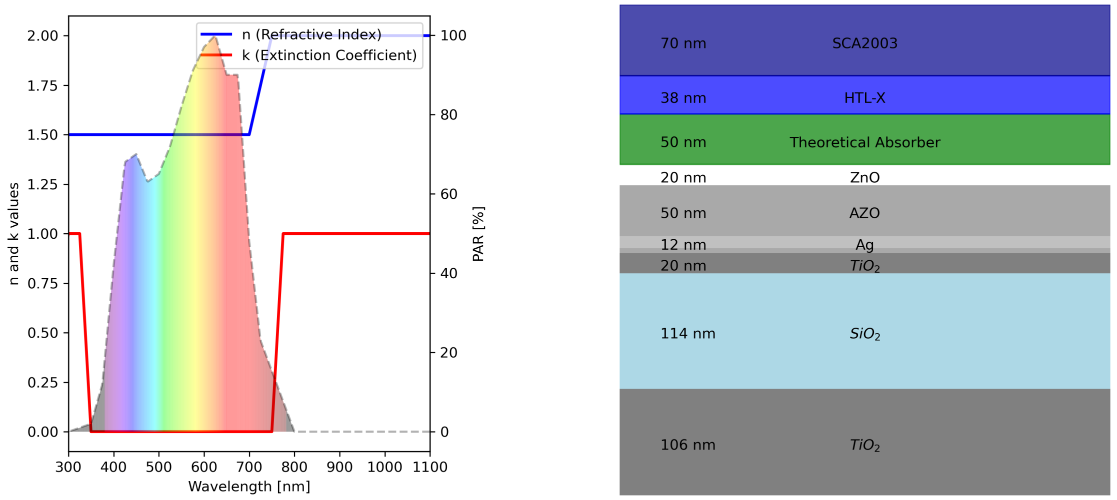

(a) (b)

Figure 6.5: (a) The refractive index (n) and extinction coefficient (k) values of the theoretical absorber as a function of wavelength, with the PAR spectrum for plant growth shown in the background. (b) Full stack of the organic solar cell, including the optimized layer thickness for each individual layer of the theoretical absorber.

Literature has shown that an electrode that mainly reflects the light in the near infrared region while transmitting most of the light in the visible region can be achieved using a Bragg reflector consisting of a single silver electrode as illustrated in Figure 6.1 and accompanied with additional dielectric metal oxide layers to optimize its optical properties [47]. This idea can be used to optimize the layer thicknesses of the solar cell stack in order to achieve the highest possible growth factor. As explained in Section 5.5 this is done using a Python script and the results are shown in Figure 6.5 b).

It is important to note that the theoretical absorber layer does not absorb light in the visible range and thus the growth factor is almost not dependent on its thickness. If the theoretical absorber is now replaced with PV-X Plus, the growth factor becomes dependent on the layer thickness of the absorber, as PV-X Plus also absorbs light in the PAR range.

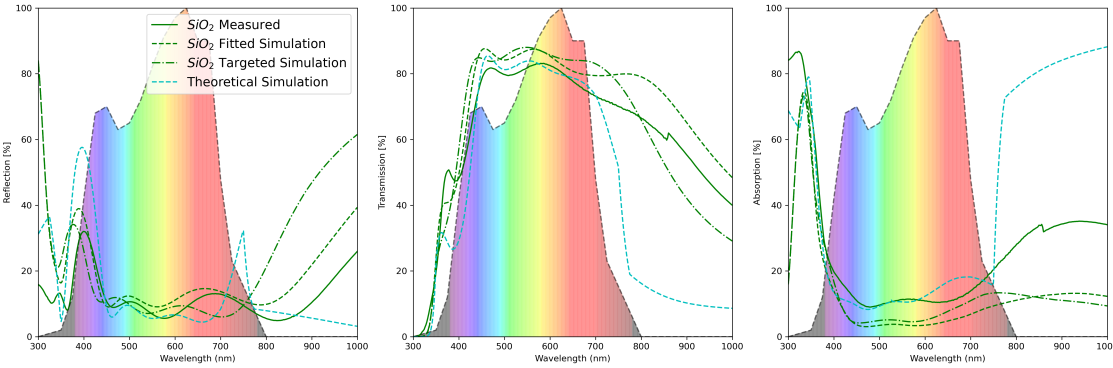

Figure 6.6: Measured RTA spectra for the SiO_2 inter-layer electrode, optimized for the theoretical absorber, compared with the targeted and fitted simulations. Deviations are most noticeable around 450 nm and beyond 700 nm. Further displayed are the simulated result for the full stack solar cell with the theoretical absorber as the blend layer.

Figure 6.6 illustrates the simulated and measured RTA data for the electrode of the stack. It is visible, that the targeted and measured spectra deviate from each other, especially in the NIR region above 750 nm. To estimate uncertainties of the sputtered layer thicknesses the simulated layers were fitted to better match the results of the sputtered electrode. The fitted thicknesses are depicted in Table 6.3 It indicates, that small variations can have a significant impact on the results.

Table 6.3: Resulting layer thicknesses of the SiO_2 inter-layer electrode optimized for a theoretical absorber from fitting to better match the experimental results. Notably, the variations are small, with differences of less than 7 nm compared to the targeted values.

Layer (Material)	**SiO_2 inter-layer [nm]**	
	Targeted	**Fitted**
AZO	43	49.5
Ag	12	9.4
AZO	5	1.1
TiO2	20	24.9
SiO_2/SiN	114	121
TiO2	106	109

The increased absorption observed in the measured electrodes compared to the simulated results can be partially attributed to variations between the n and k values used in the simulations and the actual optical properties of the sputtered layers. These properties are not only influenced by the material itself but also the sputtering rate during the process, which further fluctuates between each run. Additionally, the layer thicknesses measured using the Dektak profilometer, as explained in Section 5.4.3, are used to fit the n and k values. These measurements usually have an accuracy of about 2 nm, but deviations of up to 5 nm have been observed, which can further influence the thickness received from the simulation. Furthermore, the specific position of each substrate within the sputtering machine impacts the results, as variations in layer thicknesses, indicated by differences in color, can be observed. However, a detailed analysis of the exact impact of these variations was beyond the scope of this thesis.

The cyan colored curve in Figure 6.6 shows the simulation of the solar cell with the theoretical absorber as the blend layer. It achieves a simulated growth factor of $G = 76\,\%$ and $J_{sc} = 13.1\,\mathrm{mA\,cm^{-2}}$.

If the perfect material is replaced by PV-X Plus, we receive the following experimental results as shown in Figure 6.7. The experiments were measured with new lamp, however since the data is not compared to previous results it is not of relevance.

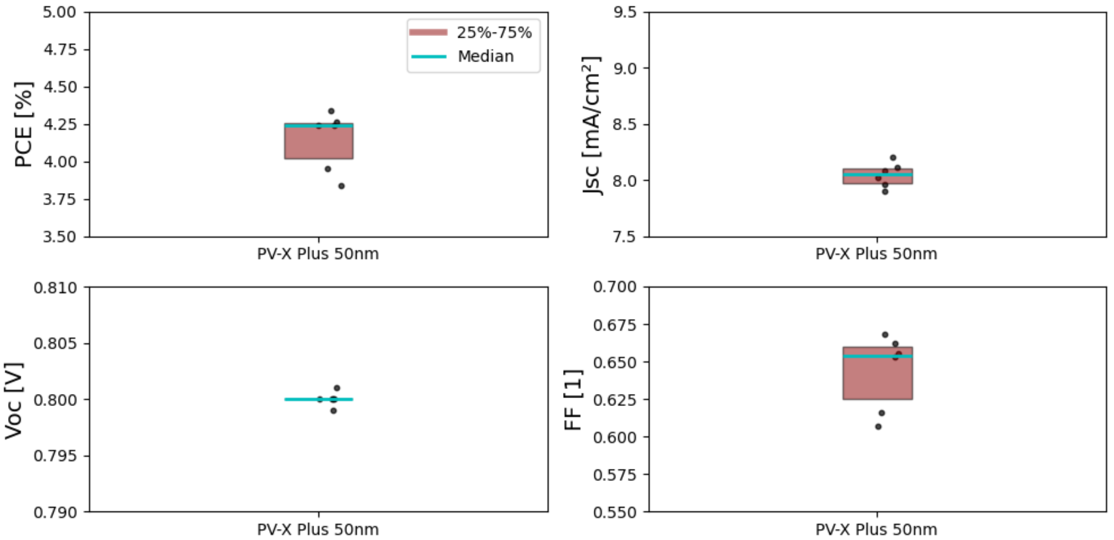

Figure 6.7: Measured characteristics for solar cells with SiO_2 inter-layer electrode optimized for the theoretical absorber. Theoretical absorber is replaced with PV-X Plus.

Considering the achieved growth factor of $G = 53.2\,\%$, it is already significantly improved compared to the single silver stack in Section 6.1. On the other hand, if compared to the theoretical absorber, it becomes clear that the absorber material is the main bottleneck to achieve both, a high transparency and high power conversion efficiency, simultaneously.

6.4 Stack Optimization for PV-X Plus

Based on the previous sections, it is clear that PV-X Plus remains the best candidate as the photoactive layer to achieve the target of of $G = 60\,\%$. For that purpose two electrodes have been designed, as shown in Figure 6.8. These electrodes have been optimized specifically for PV-X Plus, as described in Section 5.5.
It is important to mention that the n and k values used during the optimization process were taken from measurements from Leonie Pap and Bertholt Schirmacher or a database from the software Scout [52]. The expected J_{sc} and G results from the simulation are presented in Table 6.4.

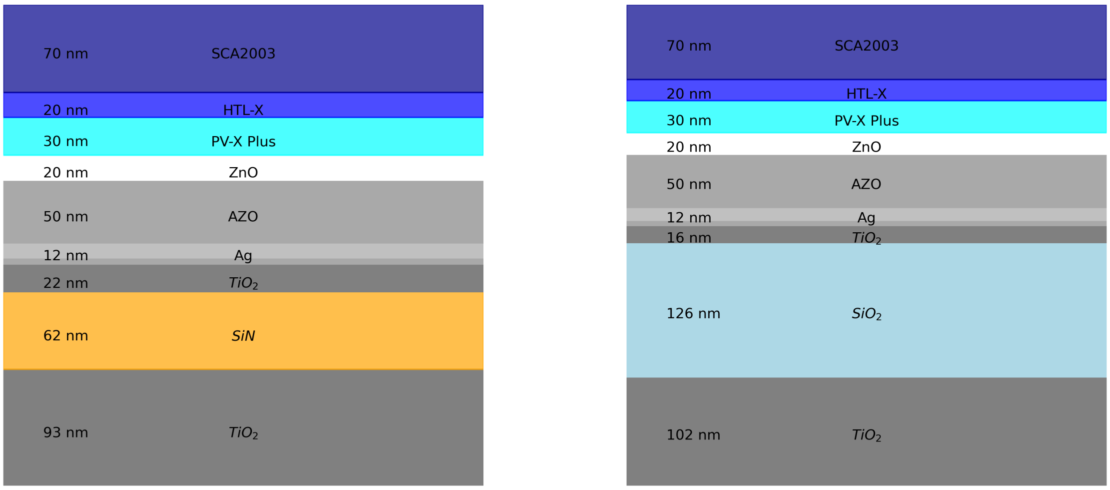

(a) (b)

Figure 6.8: Full stack organic solar cell including the layer thickness for each individual layer with a) SiN inter-layer and b) SiO_2 inter-layer, both optimized for the blend PVXplus

Table 6.4: Simulated optical and electrical results for full stack solar cells with SiN or SiO_2 inter-layer. For the Jsc prediction a internal quantum efficiency of 1 is assumed.

Parameter	SiN Inter-layer	SiO_2 Inter-layer
Jsc $[mA/cm^2]$	8.7	7.7
G [%]	60.9	63.9

If compared with each other, the expected growth factor for the SiN inter-layer electrode is lower to those for the SiO_2 inter-layer. However, since the SiN stack typically uses thinner layers, it is worth investigating if the target can be achieved, as this offers advantages for large-scale production. One industry partner recommended using thinner layers to avoid having multiple sputtering runs for one layer.

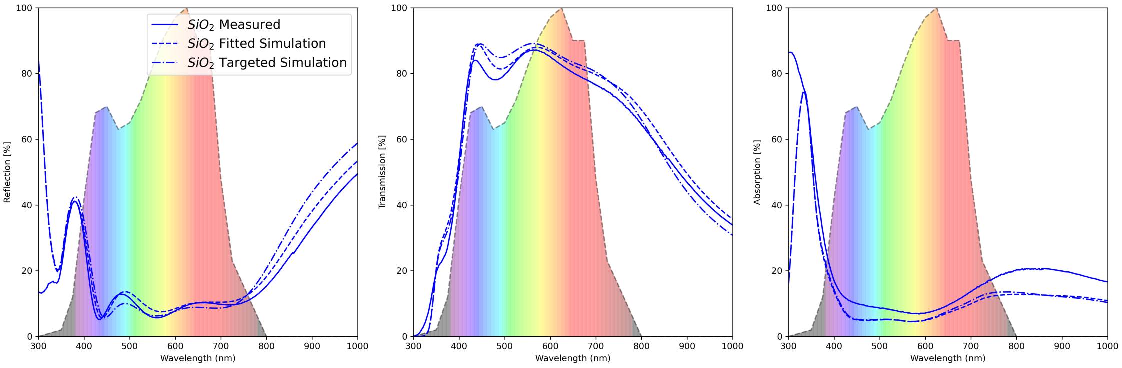

Figure 6.9: Measured RTA spectra for the SiO_2 inter-layer electrode compared with the targeted and fitted simulations. Deviations are most noticeable in the absorption around 450 nm and beyond 700 nm.

Figure 6.9 shows a comparison between the measured result of the SiO_2 inter-layer electrode and the simulation based on the layer thicknesses presented for the electrode layers in Figure 6.8 (b). The layer thicknesses were again adjusted to better match the observed results and to provide an estimate of the actual layer thicknesses that were achieved. Overall, the results align well with the simulations and the electrode clearly shows the desired high reflection in the infrared and a high transparency in the visible region. On the other hand, it can be observed that the electrode itself absorbs more light then it is anticipated by the simulations. This is especially the case at wavelengths around 450 nm and in the NIR region above 750 nm.

Similarly, Figure 6.10 illustrates the results for the SiN inter-layer electrode. Here the reflection in the NIR region and a high transparency in the visible region is achieved as well. In contrast to the SiO_2 inter-layer electrode the SiN inter-layer electrode shows a less relevant increase in light absorption, but there are still deviations around 450 nm and above 750 nm.

Nevertheless, the overall fit of the simulation is in good accordance with the measured data.

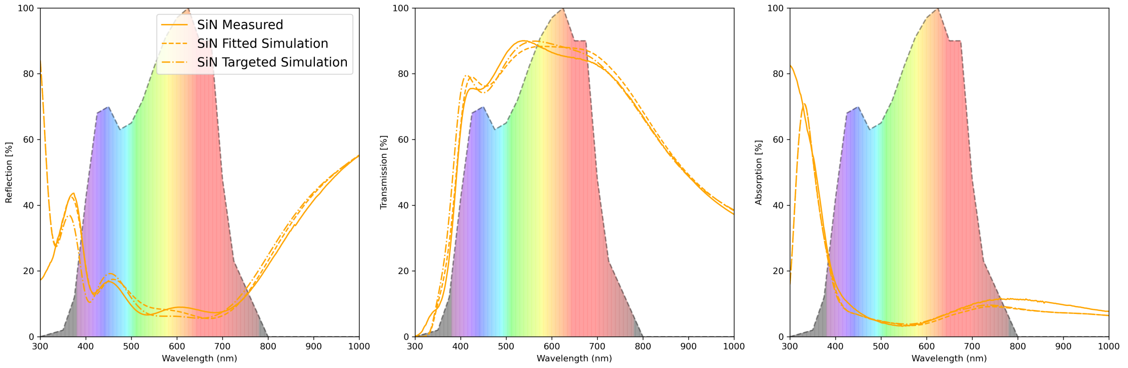

Figure 6.10: Measured RTA spectra for the SiN inter-layer electrode compared with the targeted and fitted simulations.

Table 6.5 shows the layer thicknesses when they are fitted to match the experimental results. It indicates that even small variations in layer thicknesses (less than 5 nm) can have a noticeable impact on the optical properties of the complete electrode.

Table 6.5: Resulting layer thicknesses from fitting to better match the experimental results. Notably, the variations are small, with differences of less than 5 nm compared to the targeted values.

Layer (Material)	**SiO_2 inter-layer [nm]**		**SiN inter-layer [nm]**	
	Targeted	**Fitted**	**Targeted**	**Fitted**
AZO	50	51	50	48.3
Ag	12	10.8	12	12
AZO	5	4.3	5	10
TiO_2	16	13.7	22	27
SiO_2/SiN	126	127.5	64	59
TiO_2	102	104.5	92	91.1

In order to now replicate the stacks in Figure 6.8 experimentally, it is important to investigate the impact of each layer on its own. This approach allows for a clear observation of the specific effects each layer has on the solar cell performance. If instead multiple parameters are changed simultaneously, it becomes difficult to identify which change was responsible for the observed result. Thus it avoids making wrong conclusions and ensures that the effects are understood correctly. Additionally, varying just one parameter at once is a more organized optimization method.

6.4.1 Blend Thickness Variation

The first and most important factor to be investigated, is the thickness of the blend layer on both electrode configurations. By reducing the layer thickness, it can be expected, that the short-circuit current density (J_{sc}) is reduced, due to a reduced light absorption in the thinner blend layer. Thus, also the PCE should be reduced in a comparable way. However, the FF and V_{oc} are generally expected to remain relatively constant, as they are ideally less dependent on the thickness of the active layer.

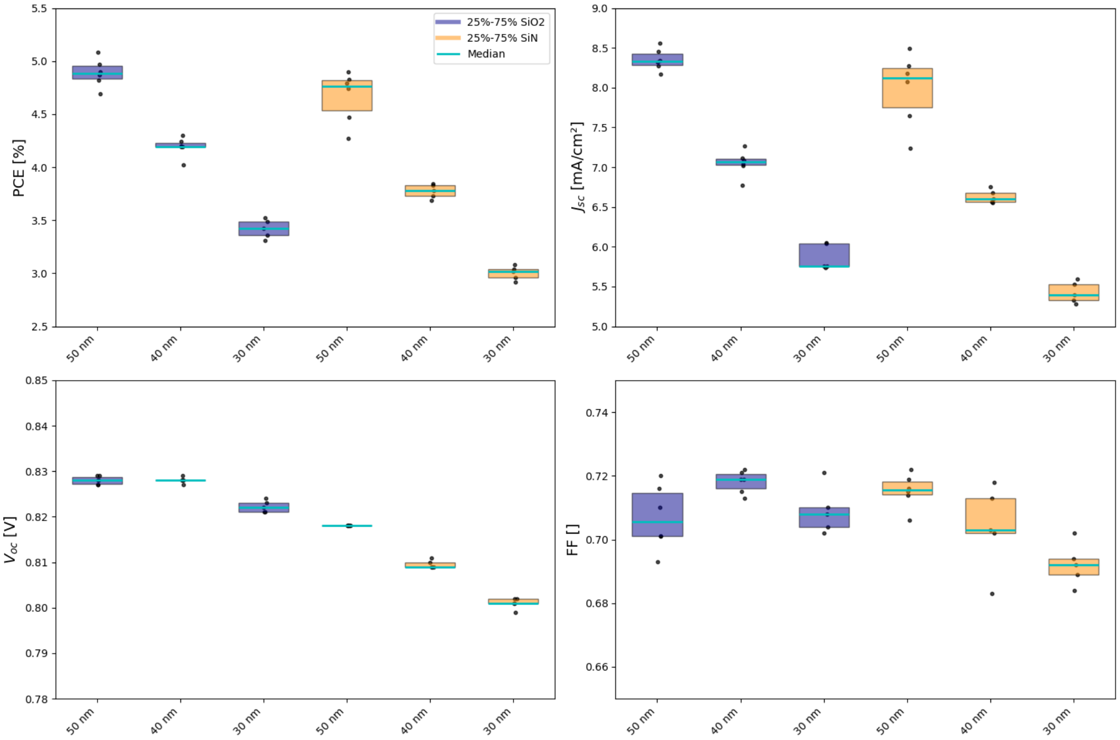

Figure 6.11: Measured characteristics for solar cells with SiO_2 and SiN inter-layers, with a thickness variation of the blend PV-X Plus. Notably, J_{sc} and PCE are reduced with thinner layers due to lower light absorption, while deviations in FF and V_{oc} remain small.

Figure 6.11 illustrates the clear expected trend in the J_{sc} and PCE reduction for both electrode configurations. In comparison to the simulations, where the SiN inter-layer was predicted to have a higher J_{sc}, the performance is worse than with the SiO_2 inter-layer.

While there is no clear trend visible in the FF and V_{oc} for the SiO_2 inter-layer electrode, these parameters are slightly decreasing for thinner layers on the SiN inter-layer electrode. This can be attributed to the increased likelihood for shunt formation. This means that due to the roughness of the surfaces, especially the sputtered electrodes, the smoothness of the blend layer can be interrupted and thus result in a direct contact between bottom and top electrode. Such contact would reduce shunt resistance, resulting in a lower FF and eventually also V_{oc}.

Table 6.6: Growth factor results for varying blend thicknesses (indicated by the thickness in nm after the electrode type). The results show that the thinnest layer on the SiO_2 electrode nearly achieves the target of $G = 60\,\%$

Substrate	SiO_2 50 nm	SiO_2 40 nm	SiO_2 30 nm	SiN 50 nm	SiN 40 nm	SiN 30 nm
G [%]	52.7	56.3	59.8	51.6	54.9	57.5

When the optical properties, as shown in Table 6.6, are also considered, it becomes clear that the electrode with the SiO_2 inter-layer is more suited to achieve the targeted growth factor. With a G of 59.8 %, the thinnest layer nearly meets the desired result. Nevertheless, the simulated results were not fully met, but since the generated current is low, the required conductivity for the top electrode can also be reduced.

Therefore, the next option to reach the target is to decrease the layer thickness of the two hole transport layers. This should reduce the parasitic absorption, but it has to be investigated, if the conductivity remains sufficiently high.

6.4.2 Hole Transport Layer Thickness Variation

The next important step is to further reduce the layer thickness of the HTL-X and SCA2003 layers, while leaving the blend thickness at 30 nm. Initial tests were conducted on glass to determine how thin these layers can be while still forming a uniform layer. Notably, the HTL-X layer is slightly thicker than originally intended in the simulation (28 nm instead of 20 nm). The goal of this reduction is to decrease parasitic absorption, particularly from the PEDOT layers, which would result in higher transparency and potentially increase the short-circuit current density as more light can reach the active layer.

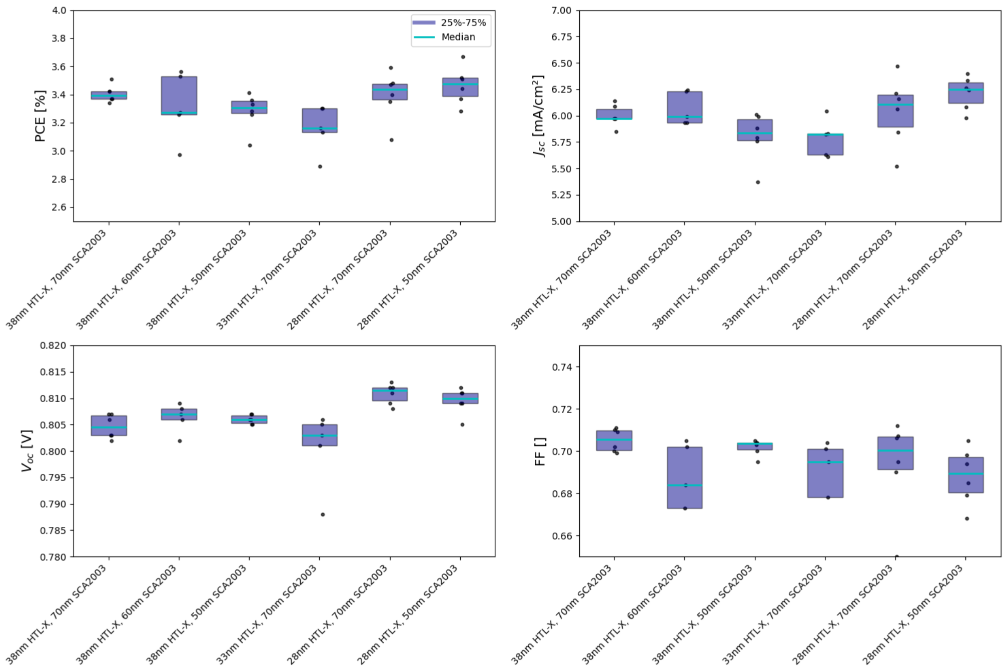

Figure 6.12: Electrical properties of HTL layer variations. No clear trends are observed, but overall the thinnest layers showing the highest PCE.

Figure 6.12 presents the electrical properties of such a HTL layer variation. Overall, no clear trends are visible. The expected reduction in parasitic absorption with a thinner SCA 2003 layer and therefore an increased J_{sc} was not observed. The thinner HTL-X layer seems to slightly improve J_{sc}, but the effect is not significant. Interestingly, it was found that despite observing little to no changes in decreasing each one of the PEDOT layers respectively, reducing both layers at the same time has the greatest effect on J_{sc} and therefore results in the highest PCE.

Considering the substrate labeled "38 nm HTL-X, 70 nm SCA 2003" in Figure 6.12 and the 30 nm PV-X Plus substrate on the SiO_2 inter-layer electrode in Figure 6.11, potential batch-to-batch variations can be estimated. For example a reduction in V_{oc} can be observed between the two substrates, even though they were produced with the same parameters. While this might be partly due to in-batch variations, as explained in Section 6.4.1, it could also result from differences that only occur between separate batches produced on different days.
For example, humidity, temperature, and oxygen levels within the glove box can vary slightly, as well as the solution concentrations of the coated materials. Especially

the blend may differ due to slow solvent evaporation during storage time or small pipetting uncertainties. Finally, minimal variations in the actual spin-coating speed and in the reference cell current calibration during IV-curve measurements can also contribute.

As there were only a limited number of full area substrates available, which are necessary for measuring RTA data and calculating G, only optical properties from the substrate with the thinnest HTL layers was investigated. The result shows a growth factor of 61.6 %.

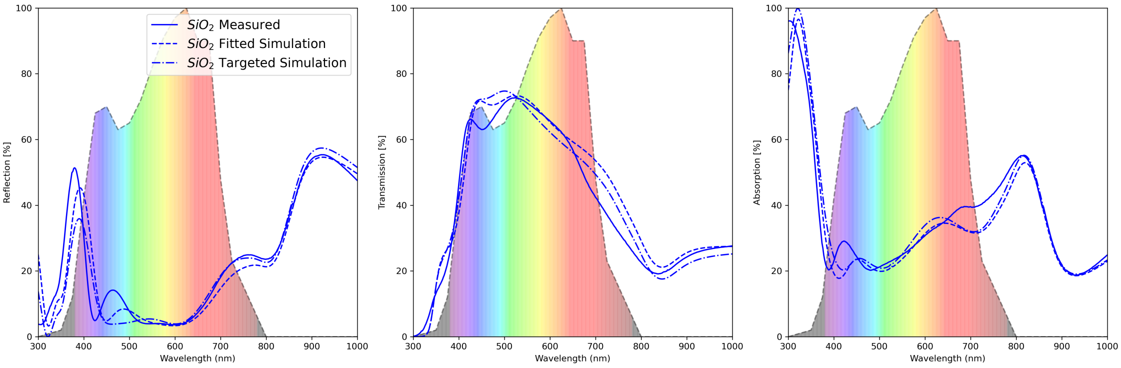

Figure 6.13: RTA spectra of the full stack, showing slight deviations between the intended and experimental results, especially around 450 nm and 700 nm.

Considering the RTA spectra of the full stack, as illustrated in Figure 6.13, the simulation is in very good agreement with the experimental results. Considering the fitted electrode from Figure 6.9 and fitting the additional layers on top, the simulation and experimental results align even closer. However, slight deviations remain, particularly in the reflection and absorption peaks around 450 nm and generally in the region around 700 nm.

Further, as these represent the best absolute results for the J_{sc}, they can be directly compared to the simulated J_{sc}. The results for the fitted layers already deviate with a $J_{sc} = 7.18\,\mathrm{mA\,cm^{-2}}$ from the targeted $J_{sc} = 7.7\,\mathrm{mA\,cm^{-2}}$ mentioned in Section 6.4. Compared with the experimental results of $J_{sc_{mean}} = 6.24\,\mathrm{mA\,cm^{-2}}$, small variations remain. It is important to note that the internal quantum efficiency for these simulations is assumed to be 1, and the remaining deviations in the RTA spectra may further increase the discrepancies. Despite this, the results show good alignment with the simulations.

One possible explanation for some of the remaining deviations in the RTA spectra is that the annealing was done stepwise. For instance, the overall annealing time for PV-X Plus adds up to 17 minutes, compared to the 10 minutes when only the single layer was annealed, which was used to determine the optical constants for the simulation. Therefore, in the following section, all layers will be annealed together for 10 minutes in the end to ensure consistency.

6.4.3 Changed Annealing Strategy and UV-Ozon Treatment

In the following it was evaluated, if a different annealing strategy, as well as additional surface cleaning of the electrode would improve the results.
The figure of merit is displayed in Figure 6.14.

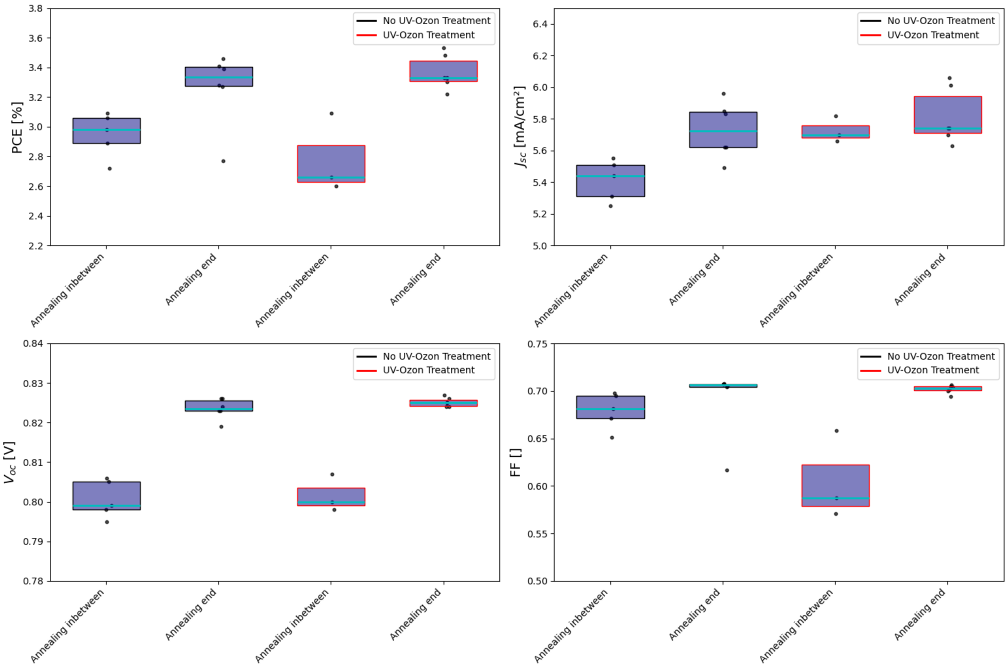

Figure 6.14: Measured electrical properties for two annealing procedures and UV treatment. Annealing all layers together improves electrical parameters, while the UV treatment shows no significant effect on the electrical performance.

The substrate labeled as "Annealing inbetween" shows a significant reduction in PCE and J_{sc} compared to the corresponding substrate in the previous experiment labeled "28 nm HTL-X, 50 nm SCA 2003". Both of them were produced with the

same parameters and should show similar results. It was later found that this was most likely due to a lamp exchange in the sun simulator, leading to an incorrect mismatch factor during the measurement as the spectrum of the new lamp was not adjusted in the mismatch calculation. Therefore the absolute values should not be considered and the focus should be rather on the relative improvements observed in this experiment. Figure 6.14 demonstrates that annealing all layers together at the end of the process improves all electrical parameters.
On the other hand Table 6.7 shows that (G) is slightly decreased from 61.6 % to 61.0 %.
The improved performance may be because the thermal stress on individual layers, especially the blend is reduced, which minimizes the risk of degradation. In Section 2.1.2 it is explained, that especially surfaces between layers form a bottleneck in the charge transport as trap states are more likely to occur.

Table 6.7: Growth factor results for two annealing procedures and UV treatment. Both annealing procedures achieve the target of $G \geq 60\,\%$, while the UV treatment significantly changes the optical properties in an undesired direction.

Substrate	In between	End	In between (UV)	End (UV)
G [%]	61.6	61.0	48.6	56.1

In contrast, the additional UV-Ozone treatment, even though it had similar electrical results, changed the optical properties significantly as seen in Table 6.7. Already after the treatment of the electrode, it was visibly changed and appeared golden. This indicates that the UV-Ozone treatment likely altered the electrode material, possibly due to oxidation, which can lead to changed optical properties of the electrode. As the stack is sensitive to changes and each layer is optimized in regards to the other layers, the modified optical properties of the electrode can have a high impact. Thus such a treatment is not recommended.

Finally, considering the RTA spectra in Figure 6.15, it becomes clear that the longer annealing time used in the previous section may have already influenced the morphology of the cell materials that were applied using spin-coating. The fitted result for the full stack align closely with the experimental data. It is again visible, that especially the absorption seem to deviate a bit more, which can probably be attributed to the electrode itself, as similar deviations between the experimental and simulated results were visible in Figure 6.9 already.

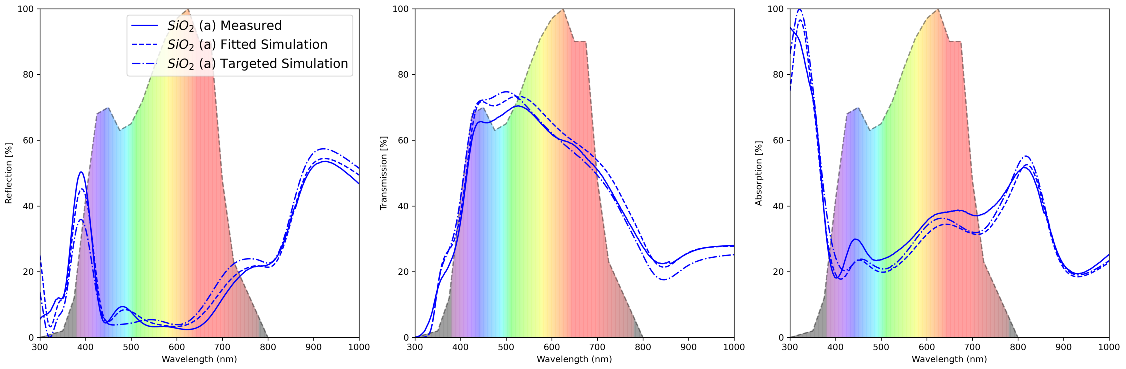

Figure 6.15: RTA spectra of the full stack for the second annealing procedure. Simulated and measured results align closely.

For further considerations the IV-curves can be taken into account. Figure 6.16 shows that in both annealing processes the difference between the reverse bias current and the short-circuit current (J_{sc}) is minimal. Nonetheless, "annealing end" results in a smaller difference between the reverse bias current and the short-circuit current, as well as higher absolute values for both.

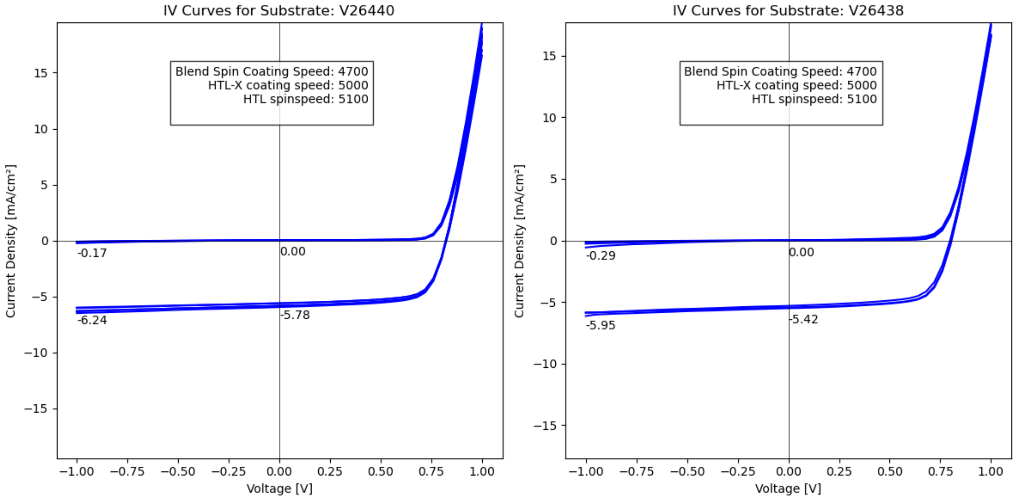

Figure 6.16: IV-curves for both annealing processes. The left graph shows annealing at the end, and the right shows annealing in-between. With annealing at the end showing a smaller difference and higher mean values for J_{sc} and reverse bias currents.

Chapter 7

Summary and Conclusion

The climate change is forcing humanity to reconsider its energy consumption and production. Modern renewable energy sources, like wind turbines, silicon based photovoltaic and hydro-power have become an important part of the solution for the energy transition. Yet they are not everywhere applicable and their environmental footprint is sometimes still significant. Therefore research in areas that offer additional benefits is necessary.

In this thesis the development of semi-transparent organic photovoltaics was investigated. Organic photovoltaics, beside having a reduced carbon footprint when it comes to large scale production they also offer the huge benefit of wavelength selective absorption, making them well suited for semi-transparent applications like tinted windows or in agrivoltaics.

A large part of the energy coming from the sun is in the infrared region, which makes it theoretically possible to achieve a reasonable power conversion efficiency (PCE) while transmitting all visible light. For agrivoltaic applications, it is important to reach a sufficient transparency level in the photosynthetically active radiation (PAR) region, in order to minimize negative effects on plant growth. This transparency can be quantified by the growth factor, which represents the weighted percentage of light transmitted through the cell, based on the wavelengths that are most relevant for plant growth. While the requirements vary for different plant species, a minimum growth factor of 60 % is recommended to support the growth of a variety of plants, for example, basil. The objective of this thesis was to design a solar cell stack that reaches the required transparency target by investigating different absorber materials and redesigning the cell stack.

As a first step, the current solar cell stack, typically used by the research group for semi-transparent organic cells in window applications, was evaluated based on the growth factor. This served as a benchmark for the following experiments.

Afterwards, several absorber materials were analyzed for their suitability in agrivoltaic applications. As the electrical performance of PCE10:COi8DFIC:PC60BM, PCE10:IEICO-2F and PV-F4801 and the simulated growth factor results were low, the originally used blend, PV-X Plus, emerged as the most suitable candidate.
A solar cell stack was simulated using a theoretical absorber, where the n and k values were chosen to ensure that it only absorbs light in the non-visible spectrum. The stack was optically modeled and optimized using Python code based on the transfer matrix method (TMM) to maximize the growth factor. This simulation demonstrated the feasibility of achieving high transparency, with a calculated growth factor of $G = 76\,\%$, assuming a well-suited theoretical absorber. The results indicate that the electrode, charge-selective hole transport layer, and electron transport layer are not limiting factors in achieving sufficient transparency to support optimal plant growth.
The optimization process using the Python script was then repeated specifically for PV-X Plus. In several experiments, the simulated stack was physically recreated. Initially, the absorber thickness was adjusted, which already showed significant improvements in transparency, while the cell remained electrically functional. A reduction in layer thickness of the two hole transport layers (HTL-X and SCA2003) resulted in a growth factor of $G = 61.6\,\%$ and a PCE of 3.5 %, successfully meeting the growth factor target of $G \geq 60\,\%$.
On the other hand, the relatively low PCE suggests that the absorber material is not optimal for this application, indicating that further research into absorber materials is necessary for organic photovoltaic systems to become a competitive alternative to silicon-based solar cells in agrivoltaic applications.
In a final experiment a second annealing strategy showed potential for additional improvements in the power conversion efficiency, while also the obtained RTA results aligned more closely with the simulations. Due to issues with the sun simulator during testing, a full validation of the effect was not possible and should be investigated in further experiments.

The findings of this thesis demonstrate that organic photovoltaics has the potential to utilize agricultural area for energy production, while minimizing the negative effect on plant growth. The achieved growth factor of $G = 61.6\,\%$ clearly meets the minimum target of $G = 60\,\%$, that was suggested by research on plant growth under shading conditions. To make organic photovoltaic systems a viable commercial product, improvements especially in the resulting PCE are necessary. This indicates, that the research focus should be on the development of absorber materials that are more beneficial for semi-transparent applications. Furthermore, several other steps are needed in order to use this technology in real-world scenarios. First, this study was limited to small laboratory cells produced with a spin-coating process. As a next step the cells should be scaled to module size and finally transition to flexible large scale substrates that can be used in a roll-to-roll production. This could make a large-scale production for the use in agrivoltaic fields possible. Secondly, the stability and lifetime, as well as encapsulation methods, have to be investigated under realistic conditions. Finally, the actual impact of semi-transparent organic photovoltaic systems on plant growth across various crops should be investigated to provide additional data for future optimizations and further improvements of these devices.

Nevertheless, this work contributes to a better understanding of how organic photovoltaic technology can be optimized in terms of its transparency and energy efficiency. The work has clearly met its target and demonstrated that it is nowadays possible to achieve sufficient transparency levels for semi-transparent organic solar cells that do not reduce the plant growth significantly, when they cover an agricultural field.

References

[1] I. P. on Climate Change (IPCC), "Summary for policymakers," in *Climate Change 2021 – The Physical Science Basis: Working Group I Contribution to the Sixth Assessment Report of the Intergovernmental Panel on Climate Change*. Cambridge University Press, 2023, pp. 3–32.

[2] M. Beniston, D. Farinotti, M. Stoffel, *et al.*, "The european mountain cryosphere: A review of its current state, trends, and future challenges," *The Cryosphere*, vol. 12, no. 2, pp. 759–794, 2018. DOI: `10.5194/tc-12-759-2018`.

[3] M. Franchini and P. M. Mannucci, "Impact on human health of climate changes," *European Journal of Internal Medicine*, vol. 26, no. 1, pp. 1–5, 2015, ISSN: 0953-6205. DOI: `https://doi.org/10.1016/j.ejim.2014.12.008`.

[4] International Energy Agency, *World energy outlook 2023 – analysis*, 2023. [Online]. Available: `https://www.iea.org/reports/world-energy-outlook-2023`.

[5] International Energy Agency, *Electricity Market Report – Update 2023*, Licence: CC BY 4.0, Paris, 2023. [Online]. Available: `https://www.iea.org/reports/electricity-market-report-update-2023`.

[6] S. Bobba, S. Carrara, J. Huisman, F. Mathieux, and C. Pavel, *Critical raw materials for strategic technologies and sectors in the eu*, 2020. DOI: `10.2873/58081`.

[7] E. Commission, J. R. Centre, O. Eulaerts, M. Grabowska, and M. Bergamini, *Clean Energy Technology Observatory, Early stage technologies in the field of energy*. Publications Office of the European Union, 2024. DOI: `doi/10.2760/711`.

[8] International Energy Agency (IEA), *World energy outlook 2022*, `https://www.iea.org/reports/world-energy-outlook-2022`, Licence: CC BY 4.0 (report); CC BY NC SA 4.0 (Annex A), Paris, 2022.

[9] S. Bampinioti, N. Christakou, B. Paulitz, *et al.*, *Land: A Crucial Resource for the Energy Transition*, Accessed: August 15, 2024, 2023. [Online]. Available: `https://www.mckinsey.com/industries/electric-power-and-natural-gas/our-insights/land-a-crucial-resource-for-the-energy-transition`.

[10] S. Schlömer, T. Bruckner, L. Fulton, *et al.*, "Annex iii: Technology-specific cost and performance parameters," in *Climate Change 2014: Mitigation of Climate Change. Contribution of Working Group III to the Fifth Assessment Report of the Intergovernmental Panel on Climate Change*, O. Edenhofer, R. Pichs-Madruga, Y. Sokona, *et al.*, Eds., Cambridge, United Kingdom and New York, NY, USA: Cambridge University Press, 2014.

[11] Z. Hu, J. Wang, X. Ma, *et al.*, "A critical review on semitransparent organic solar cells," *Nano Energy*, vol. 78, p. 105 376, 2020, ISSN: 2211-2855. DOI: `https://doi.org/10.1016/j.nanoen.2020.105376`.

[12] L. Pap, B. Schirmacher, E. Bloch, *et al.*, "Improved light utilization efficiency for an ito-free semitransparent organic solar cell using a multilayer silver back electrode as infrared mirror," *Solar RRL*, vol. 7, no. 21, p. 2 300 561, 2023. DOI: `https://doi.org/10.1002/solr.202300561`.

[13] M. P. Tsang, G. W. Sonnemann, and D. M. Bassani, "Life-cycle assessment of cradle-to-grave opportunities and environmental impacts of organic photovoltaic solar panels compared to conventional technologies," *Solar Energy Materials and Solar Cells*, vol. 156, pp. 37–48, 2016, Life cycle, environmental, ecology and impact analysis of solar technology, ISSN: 0927-0248. DOI: `https://doi.org/10.1016/j.solmat.2016.04.024`.

[14] National Renewable Energy Laboratory, *Interactive best research-cell efficiency chart*, `https://www.nrel.gov/pv/interactive-cell-efficiency.html`, Accessed: 2024-05-26, 2024.

[15] M. Kaltenbrunner, M. S. White, E. D. Głowacki, *et al.*, "Ultrathin and lightweight organic solar cells with high flexibility," *Nature Communications*, vol. 3, p. 770, 2012. DOI: `10.1038/ncomms1772`.

[16] K. Fukuda, K. Yu, and T. Someya, "The future of flexible organic solar cells," *Advanced Energy Materials*, vol. 10, no. 25, p. 2 000 765, 2020. DOI: `https://doi.org/10.1002/aenm.202000765`.

[17] J. Sun and J. J. Jasieniak, “Semi-transparent solar cells,” *Journal of Physics D: Applied Physics*, vol. 50, no. 9, p. 093 001, 2017. DOI: 10.1088/1361-6463/aa53d7.

[18] E. J. Stallknecht, C. K. Herrera, C. Yang, *et al.*, “Designing plant–transparent agrivoltaics,” *Scientific Reports*, vol. 13, no. 1, p. 1903, 2023, ISSN: 2045-2322. DOI: 10.1038/s41598-023-28484-5.

[19] H. Shi, R. Xia, G. Zhang, H.-L. Yip, and Y. Cao, “Spectral engineering of semitransparent polymer solar cells for greenhouse applications,” *Advanced Energy Materials*, vol. 9, no. 5, p. 1 803 438, 2019. DOI: https://doi.org/10.1002/aenm.201803438.

[20] D. Wang, H. Liu, Y. Li, *et al.*, “High-performance and eco-friendly semitransparent organic solar cells for greenhouse applications,” *Joule*, vol. 5, no. 4, pp. 945–957, 2021, ISSN: 2542-4785. DOI: 10.1016/j.joule.2021.02.010.

[21] L. Hirst, “1.14 - principles of solar energy conversion,” in *Comprehensive Renewable Energy*, A. Sayigh, Ed., Oxford: Elsevier, 2012, pp. 293–313, ISBN: 978-0-08-087873-7. DOI: https://doi.org/10.1016/B978-0-08-087872-0.00115-3.

[22] A.-E. Becquerel, “Mémoire sur les effets électriques produits sous l’influence des rayons solaires,” *Comptes Rendus de l’Académie des Sciences*, vol. 9, pp. 561–567, 1839.

[23] P. Würfel and U. Würfel, *Physics of Solar Cells: From Basic Principles to Advanced Concepts*. John Wiley & Sons, 2016.

[24] A. Köhler and H. Bässler, *Electronic Processes in Organic Semiconductors: An Introduction*. John Wiley & Sons, 2015.

[25] O. Wodo, S. Tirthapura, S. Chaudhary, and B. Ganapathysubramanian, “A graph-based formulation for computational characterization of bulk heterojunction morphology,” *Organic Electronics*, vol. 13, no. 6, pp. 1105–1113, 2012, ISSN: 1566-1199. DOI: https://doi.org/10.1016/j.orgel.2012.03.007.

[26] M. List, *Advanced electrical and optical characterization of recombination in organic solar cells*, 2019. DOI: 10.24406/publica-fhg-282720.

[27] J. Lian, Y. Yuan, E. Peng, and J. Huang, "Interfacial layers in organic solar cells," in *Organic and Hybrid Solar Cells*, H. Huang and J. Huang, Eds. Cham: Springer International Publishing, 2014, pp. 121–176. DOI: `10.1007/978-3-319-10855-1_5`.

[28] A. Way, J. Luke, A. D. Evans, *et al.*, "Fluorine doped tin oxide as an alternative of indium tin oxide for bottom electrode of semi-transparent organic photovoltaic devices," *AIP Advances*, vol. 9, no. 8, p. 085 220, Aug. 2019, ISSN: 2158-3226. DOI: `10.1063/1.5104333`.

[29] X. Ma, Y. Mi, F. Zhang, *et al.*, "Efficient ternary polymer solar cells with two well-compatible donors and one ultranarrow bandgap nonfullerene acceptor," *Advanced Energy Materials*, vol. 8, no. 11, p. 1 702 854, 2018. DOI: `https://doi.org/10.1002/aenm.201702854`.

[30] M. A. Green, "Self-consistent optical parameters of intrinsic silicon at 300 k including temperature coefficients," *Solar Energy Materials and Solar Cells*, vol. 92, no. 11, pp. 1305–1310, 2008.

[31] S. Alam, S. Sim, M. Q. Li, B.-J. Chang, and J. Lee, "Recent progress in semi-transparent organic solar cells: Photoabsorbent materials and design strategies," *Micromachines*, vol. 15, no. 4, 2024. DOI: `10.3390/mi15040493`.

[32] C. Yang, D. Liu, M. Bates, M. C. Barr, and R. R. Lunt, "How to accurately report transparent solar cells," *Joule*, vol. 3, no. 8, pp. 1803–1809, 2019, ISSN: 2542-4351. DOI: `https://doi.org/10.1016/j.joule.2019.06.005`.

[33] H. Shi, R. Xia, G. Zhang, H.-L. Yip, and Y. Cao, "Spectral engineering of semitransparent polymer solar cells for greenhouse applications," *Advanced Energy Materials*, vol. 9, no. 5, 2018. DOI: `10.1002/aenm.201803438`.

[34] K. J. McCree, "The action spectrum, absorptance and quantum yield of photosynthesis in crop plants," *Agricultural Meteorology*, vol. 9, pp. 191–216, 1972, ISSN: 0002-1571. DOI: `10.1016/0002-1571(71)90022-7`.

[35] A. D. Vos, "Detailed balance limit of the efficiency of tandem solar cells," 1980. DOI: `10.1088/0022-3727/13/5/018`.

[36] L. Duan, B. Hoex, and A. Uddin, "Progress in semitransparent organic solar cells," *Solar RRL*, vol. 5, no. 5, p. 2 100 041, 2021. DOI: `https://doi.org/10.1002/solr.202100041`.

[37] N. Gruda, M. Bisbis, and J. Tanny, “Impacts of protected vegetable cultivation on climate change and adaptation strategies for cleaner production – a review,” *Journal of Cleaner Production*, vol. 225, pp. 324–339, 2019, ISSN: 0959-6526. DOI: `https://doi.org/10.1016/j.jclepro.2019.03.295`.

[38] S. Amaducci, X. Yin, and M. Colauzzi, “Agrivoltaic systems to optimise land use for electric energy production,” *Applied Energy*, vol. 220, pp. 545–561, 2018, ISSN: 0306-2619. DOI: `https://doi.org/10.1016/j.apenergy.2018.03.081`.

[39] M. Trommsdorff, J. Kang, C. Reise, *et al.*, “Combining food and energy production: Design of an agrivoltaic system applied in arable and vegetable farming in germany,” *Renewable and Sustainable Energy Reviews*, vol. 140, p. 110 694, 2021, ISSN: 1364-0321. DOI: `https://doi.org/10.1016/j.rser.2020.110694`.

[40] S. Schindele, M. Trommsdorff, A. Schlaak, *et al.*, “Implementation of agrophotovoltaics: Techno-economic analysis of the price-performance ratio and its policy implications,” *Applied Energy*, vol. 265, p. 114 737, 2020, ISSN: 0306-2619. DOI: `https://doi.org/10.1016/j.apenergy.2020.114737`.

[41] J. Krc *et al.*, *Optical modeling and simulation of thin-film photovoltaic devices.* Crc Press, 2013.

[42] E. Hecht, *Optics.* Pearson Education, Incorporated, 2017, ISBN: 9780133977226. [Online]. Available: `https://books.google.de/books?id=ZarLoQEACAAJ`.

[43] M. Ware and J. Peatross, *Physics of Light and Optics (Black & White).* Brigham Young University, Department of Physics, 2015, ISBN: 9781312929272. [Online]. Available: `https://books.google.de/books?id=Cw2LDwAAQBAJ`.

[44] M. S. Islam, “In-depth analysis of organic solar cells using transport equation and optical transfer matrix method with detailed analytical derivations,” *Energies*, vol. 14, p. 735, Jan. 2021. DOI: `10.3390/en14030735`.

[45] N. R. E. L. (NREL), *Reference air mass 1.5 spectra*, Accessed: 2024-09-21, 2012. [Online]. Available: `https://www.nrel.gov/grid/solar-resource/spectra-am1.5.html`.

[46] L. Jiang, S. Zhou, J. Yang, *et al.*, “Near-infrared light responsive tio2 for efficient solar energy utilization,” *Advanced Functional Materials*, vol. 32, no. 12, p. 2 108 977, 2022. DOI: `https://doi.org/10.1002/adfm.202108977`.

[47] L. Pap, B. Schirmacher, E. Bloch, C. Baretzky, B. Zimmermann, and U. Würfel, "Dielectric bragg reflector as back electrode for semi-transparent organic solar cells with an average visible transparency of 52%," *Solar RRL*, vol. n/a, no. n/a, p. 2 400 399, 2024. DOI: `https://doi.org/10.1002/solr.202400399`.

[48] W. Xu and F. Gao, "The progress and prospects of non-fullerene acceptors in ternary blend organic solar cells," *Mater. Horiz.*, vol. 5, pp. 206–221, 2 2018. DOI: `10.1039/C7MH00958E`.

[49] W. Li, Y. Xu, X. Meng, *et al.*, "Visible to near-infrared photodetection based on ternary organic heterojunctions," *Advanced Functional Materials*, vol. 29, Mar. 2019. DOI: `10.1002/adfm.201808948`.

[50] K. Khandelwal, S. Biswas, A. Mishra, and G. D. Sharma, "Semitransparent organic solar cells: From molecular design to structure–performance relationships," *J. Mater. Chem. C*, vol. 10, pp. 13–43, 1 2022. DOI: `10.1039/D1TC04569E`.

[51] Y. Liu, P. Cheng, T. Li, *et al.*, "Unraveling sunlight by transparent organic semiconductors toward photovoltaic and photosynthesis," *ACS Nano*, vol. 13, no. 2, pp. 1071–1077, 2019. DOI: `10.1021/acsnano.8b08577`.

[52] W. Theiss, *Scout - optical modeling software*, `https://www.mtheiss.com/docs/scout2/?materials.htm`, Accessed: 2024-09-16, 2024.

Appendix

A.1 Physical constants

Symbol	Quantity	Value
c_0	Speed of light in vacuum	$299\,792\,458\,\mathrm{m/s}$
h	Planck constant	$6.62607015 \times 10^{-34}\,\mathrm{J/Hz}$
ϵ_0	Vacuum electric permittivity	$8.8541878128 \times 10^{-12}\,\mathrm{F/m}$
μ_0	Vacuum magnetic permeability	$1.25663706212 \times 10^{-6}\,\mathrm{N/A^2}$
k_B	Boltzmann constant	$1.380649 \times 10^{-23}\,\mathrm{J/K}$
e	Elementary charge	$1.602176634 \times 10^{-19}\,\mathrm{C}$
m_e	Electron mass	$9.10938356 \times 10^{-31}\,\mathrm{kg}$

A.2 Abbreviations

Ag Silver.

AM 1.5G Air Mass 1.5 Global, a standard spectrum used for solar cell testing.

APS Announced Pledges Scenario.

AVT Average Visible Transmission.

AZO Aluminum doped Zinc Oxide.

BHJ Bulk Heterojunction.

DBR Dielectric Bragg Reflector.

DOS Density of States.

DS Double Silver Electrode.

EQE External Quantum Efficiency.

ETL Electron Transport Layer.

FF Fill Factor.

G Growth Factor.

HOMO Highest Occupied Molecular Orbital.
HTL Hole Transport Layer.

IQE Internal Quantum Efficiency.
ITO Indium Tin Oxide.
IV Current-Voltage.

$\mathbf{J_{sc}}$ Short-Circuit Current Density.
JV-curve Current-Voltage Characteristic Curve.

LEDs Light-Emitting Diodes.
LUE Light Utilization Efficiency.
LUMO Lowest Unoccupied Molecular Orbital.

MPP Maximum Power Point.

NIR Near Infra Red.
NZE Net Zero Emissions by 2050 Scenario.

OSC Organic Solar Cell.

PAR Photosynthetically Active Radiation.
PCE Power Conversion Efficiency.
PEDOT A conjugated polymer formed from 3,4-ethylenedioxythiophene (EDOT) monomers.

PV Photovoltaic.

RTA Reflection Transmission Absorption.

SiN Silicon Nitride.
$\mathbf{SiO_2}$ Silicon Dioxide.
SS Single Silver Electrode.
ST-OSC Semi Transparent Organic Solar Cell.
STEPS Stated Policies Scenario.

$\mathbf{TiO_2}$ Titanium Dioxide.
TMM Transfer-Matrix Method.

UV Ultra Violet.
UV-VIS Ultraviolet-Visible Spectroscopy.
UV-VIS-NIR Ultraviolet-Visible-Near Infrared.

$\mathbf{V_{oc}}$ Open Circuit Voltage.

ZnO Zinc Oxide.

Acknowledgements

I would like to thank Prof. Federico Bella from Politecnico di Torino for giving me the opportunity to pursue my master's thesis in Germany on a topic I am truly passionate about.

I am also grateful to Dr. Uli Würfel and Dr. Birger Zimmermann for allowing me to conduct my research at Fraunhofer ISE. Your guidance deepened my understanding of solar cells, and I appreciate the chance to contribute to this field.

A big thank you to my supervisor Leonie Pap for her constant help, valuable supervision, and kind approach. Working with you was a pleasure, and your guidance was crucial to this thesis. I would also like to thank Mathias List, Clemens Baretzky, and Nico Glissman for their valuable scientific advice and support. Additionally, I'd like to thank my colleagues at FMF and ISE for their support, motivation, and the good times we shared over the last seven months. You made this experience both enjoyable and productive.

To my friends from my master's studies in Barcelona and Torino, my friends back home in Germany, and my girlfriend: thank you for your support during this intense time. Your presence helped me get through this challenging time and I truly appreciate it.

Finally, I want to thank my family, especially my parents, for their emotional and financial support. You made sure I could fully focus on my studies, and for that, I'm deeply grateful.